Theor. Comput. Fluid Dyn. manuscript No.
(will be inserted by the editor)

An Immersed Lifting and Dragging Line Model for the Vortex Particle-Mesh Method

Denis-Gabriel Caprace · Grégoire Winckelmans · Philippe Chatelain

Received: 3 July 2019 / Accepted: 14 December 2019

Abstract The numerical study of the wake of full scale slender devices such as aircraft wings and wind turbine blades requires high-fidelity large eddy simulation tools. The broad spectrum of scales involved entails the use of coarse-grain models for the devices. Actuator disk or line methods have been developed for that purpose, and are to date the most employed in that context. These methods transfer the force from the device to the fluid using 3-D mollification functions. A novel Immersed Lifting and Dragging Line method is here presented, together with its implementation in a hybrid Vortex Particle-Mesh flow solver. The line models the effect of blades or wings on the flow through the generation of vorticity, in a Lagrangian manner. This has several advantages over the treatment inherent to actuator methods: the absence of mollification in the spanwise direction and the relaxation of the classical Courant–Friedrichs–Lewy condition contribute to keeping the accuracy and the efficiency at a high level. The method is thoroughly verified against theory using results on various airfoils and wings. Finally, the efficiency of the approach is illustrated with the simulation of the wake of an elliptical wing. The role of parasitic drag in the development of wake instabilities is pointed out, by comparing configurations with none, moderate and high profile drag. In the last case, the simulation captures the fine scales vortex dynamics and the establishment of a turbulent wake over a length of 30 wing spans.

Keywords vortex particle-mesh method · wake · large eddy simulation · elliptical wing · lifting line · drag model

1 Introduction

Wake flows have known a constantly renewed interest over the last decades, ranging from the vortical wake of aircraft and rotorcraft to the complex interactions between turbines in wind farms. The behavior of wake structures, and their decay, is indeed capital for the prediction of the performances of aerodynamic devices such as wings and blades, especially when they interact with a wake produced by another such device. It is therefore essential to develop tools able to characterize the generation of the fine vortical structures shed by those devices, their rollup into vortices, their advection over large distances and their subsequent instabilities and transition to turbulence, which all drive the trajectory and the demise of the wake.

Denis-Gabriel Caprace · Grégoire Winckelmans · Philippe Chatelain
Institute of Mechanics, Materials and Civil Engineering (iMMC), Université catholique de Louvain (UCLouvain), 2 Place du Levant, L5.04.03, Louvain-la-Neuve, B-1348, Belgium

Denis-Gabriel Caprace, F.R.S. - FNRS research aspirant fellow
ORCID: 0000-0002-6251-9129
E-mail: denis-gabriel.caprace@uclouvain.be

Grégoire Winckelmans, full professor
ORCID: 0000-0001-9722-2264

Philippe Chatelain, professor
ORCID: 0000-0001-9891-5265

As reported in recent reviews [1,14], high fidelity wake studies have recourse to Large Eddy Simulation (LES), due to the high Reynolds numbers involved. The aerodynamic devices are also commonly accounted for through coarser models, as the high computational cost associated with wall-resolved simulations is incompatible with the need for simulating the unsteady wake over large distances.

In that respect, it was proposed to replace the effect of the device on the flow by a body force, such as in the Actuator Line Method (ALM), presented e.g. in [40,18]. The forces, which are evaluated using local variables (mainly the velocity and the angle of attack) and a model for the airfoil aerodynamics, are distributed along the blade center line. Because these forces need to be captured on the computational grid, their support (i.e. the line) must be regularized so that each contribution to the forces spreads over several computational cells. This regularization involves a kernel function which describes the spacial extent of the distribution, and is referred to as 'mollification'.

The influences of the parameters of the kernel (usually, 3-D Gaussian) were investigated in [39,20,25]. The results were shown to be highly sensitive to mollification characteristics, as they affect the size and the strength of the shed structures. Additionally, the spanwise smearing of the actual force distribution was identified as the source of the largest errors, especially in the tip region, when compared to wall resolved simulations. Guidelines were proposed to minimize these errors, and further developments led to the Advanced Actuator Line (AAL) method [9] and the Actuator Curve Embedding (ACE) technique [21]. Reducing (or completely removing) the mollification in the spanwise direction indeed greatly enhances the tip behavior, as conceptually demonstrated in [3] by introducing kernels of various shapes and sizes in the Prandtl Lifting Line theory.

Nevertheless, mollification cannot be completely removed in an ALM, and the accuracy is thus intrinsically conditioned by the use of sufficiently fine grids, which allow for small size mollification kernels. Recently, filtered ALMs were introduced in [26], and a similar concept of correction for tip smearing was developed in [13,27]. By altering the local velocity measured on the line, the effect of the mollification can be reduced. However, by doing so, the connection between the flow structures and the forces measured on the line is lost: the signature of the line in the flow does not correspond to the force evaluated on the line.

In an attempt to work around some of these issues, we propose a novel Immersed Lifting and Dragging Line (ILDL) model. The latter is quite similar to an ALM as regards the aerodynamics model; yet, instead of distributing the forces on a grid, the ILDL readily takes care of the generation of the vorticity. It is specifically designed to avoid the spanwise mollification of that vorticity; the method only requires smoothing in the direction perpendicular to the local flow velocity and to the spanwise direction.

The ILDL is based on the purely lifting line model already developed and used in [4,6,7] and [2] for the high-fidelity simulation of wind turbine and rotorcraft wakes. It is here further enhanced to account for the signature of the airfoil parasitic drag in the wake, in a way that ensures the consistency between the forces computed on the line and those imparted to the fluid. It relies on a Vortex-Particle Mesh (VPM) flow solver which combines the advantages of a Vortex Particle method for the advection of the vorticity under a Lagrangian framework, and the efficiency of a grid-based (Eulerian) method for computationally intensive tasks. Advantageously, the inherently Lagrangian treatment of the vortex particles enables the method to run at Courant–Friedrichs–Lewy (CFL) numbers sensibly higher than those typical of actuator methods (imposed by the necessity of capturing the contribution of each cell to the integral of the source term in more than one time step). VPM methods also exploit the compactness of vorticity through the use of the vorticity-velocity formulation of the Navier-Stokes equation, and offer interesting numerical qualities of low dispersion and dissipation. Recent implementation of VPM methods can be found e.g. in [44,5,35,28,24].

In this work, we present the ILDL and its implementation in the VPM framework. We first briefly recall the VPM method in Section 2, with a focus on the advances that enable scalable LES. Then, the ILDL itself is detailed in Section 3, where we explain how the bound and shed vorticity is handled. The rest of the paper is dedicated to show that the present numerical method is fully consistent with the PLL theory (or eventually its mollified counterpart), and is capable of producing a genuine wake that correctly captures the flow physics. In order to verify this statement, results of the simulations of 2-D airfoils and 3-D wings are presented in Sections 4.1 and 4.2, and compared to those from theoretical models. The consistency of the flow structures shed by the ILDL model is also assessed, in order to guarantee that the correct force is applied on the fluid. Finally, as an application, the VPM method and the ILDL are used in Section 5 to simulate the wake of an elliptical wing. Three simulations illustrate how the lift and drag-induced vortex structures influence the wake dynamics, for a wing with different parasitic drag settings. The paper is closed with some conclusions in Section 6.

2 The Vortex Particle-Mesh method

The Vortex Particle-Mesh (VPM) method is based on the velocity ($\mathbf{u}$) - vorticity ($\boldsymbol{\omega} = \nabla \wedge \mathbf{u}$) formulation of the Navier-Stokes equations for incompressible flow ($\nabla \cdot \mathbf{u} = 0$):

$$\frac{D\boldsymbol{\omega}}{Dt} = (\boldsymbol{\omega} \cdot \nabla)\,\mathbf{u} + \nu \nabla^2 \boldsymbol{\omega} + \nabla \cdot \mathbf{T}^M \tag{1}$$

where $\frac{D}{Dt}$ denotes the Lagrangian derivative, ν the kinematic viscosity, and $\mathbf{T}^M$ the sub-grid scales (SGS) stress tensor. The velocity field is $\mathbf{u} = \mathbf{U}_\infty + \mathbf{u}_\omega$, where $\mathbf{u}_\omega$ is recovered from the vorticity through the Poisson equation

$$\nabla^2 \mathbf{u}_\omega = -\nabla \wedge \boldsymbol{\omega}\ . \tag{2}$$

The vorticity field is discretized by means of Lagrangian particles, each characterized by a position $\mathbf{x}_p$, a material volume V_p and a strength $\boldsymbol{\alpha}_p = \int_{V_p} \boldsymbol{\omega} d\mathbf{x}$. This Lagrangian framework provides low dispersion and dissipation errors [12,45].

In order to maintain accuracy in time, one must however prevent particles to deplete some regions of the flow or cluster in others. The particle set is hence periodically (every 5 time steps) replaced by a new set on the cartesian mesh: this procedure is called remeshing [23,33,11]. It involves the use of high order interpolation [36], here the kernel M_4' [30].

The hybrid character of the VPM method resides in the use of the mesh to improve the computational efficiency. When needed, the particle quantities are interpolated onto the mesh and finite differences permit the straightforward evaluation of the differential operators of the RHS of Eq. (1). The Poisson problem of Eq. (2) is also solved on the mesh. This is achieved using the Fourier-based solver of [5,8], which exhibits a second-order convergence. The solver is here improved to cope with unbounded and inflow/outflow directions, as detailed in Appendix C.. The results are then interpolated back at the particle locations. The advection of the particles and the update of their strength is performed using a third order Runge-Kutta time integration scheme.

In order to support LES, the regularized variational model in [19] is used, where the SGS model only acts on the "resolved small scales vorticity field" $\boldsymbol{\omega}^s$,

$$\mathbf{T}^M = \nu_{SGS} \left(\nabla \boldsymbol{\omega}^s - (\nabla \boldsymbol{\omega}^s)^T \right), \tag{3}$$

where $\boldsymbol{\omega}^s$ is obtained using efficient iterative filtering, also performed using the mesh. The divergence of $\mathbf{T}^M$ is then obtained as

$$\nabla \cdot \mathbf{T}^M = -\nabla \wedge \left(\nu_{SGS} \nabla \wedge \boldsymbol{\omega}^s \right). \tag{4}$$

The eddy viscosity is evaluated as $\nu_{SGS} = C_r^{(n)} \Delta^2 \left(2\mathbf{S} : \mathbf{S}\right)^{1/2}$, where $\mathbf{S}$ is the strain rate of the velocity field, Δ is the mesh size h, and $C_r^{(n)}$ is calibrated according to [10].

As such, the particle discretization of the vorticity field does not preserve its solenoidal character ($\nabla \cdot \boldsymbol{\omega} \neq 0$). Therefore, the vorticity field is periodically (every 20 time steps) reprojected onto a solenoidal space [11,5]. This amounts to compute the correction ∇A, and add it to the current vorticity field which might have progressively lost its solenoidal property. The scalar field A is thus obtained from solving $\nabla^2 A = -\nabla \cdot \boldsymbol{\omega}$ on the mesh, such that the corrected vorticity field $\boldsymbol{\omega} + \nabla A$ is divergence free. In order to avoid perturbations of the well-controlled bound and shed vorticity of the lifting and dragging line model (as explained in the next section), the evaluation of $\nabla \cdot \boldsymbol{\omega}$ is not performed in the region close to the line. In this region though, the solenoidal property is ensured by the model itself.

We refer to [5] for an extensive description of the Vortex Particle Mesh method and its implementation on large parallel architectures, using the open-source *PPM library* [37].

3 Immersed Lifting and Dragging Line (ILDL) method

We account for the generation of vorticity along the slender devices through a lifting line model inspired from the Prandtl Lifting Line theory [34], which is here further extended to account for the airfoil parasitic drag. In this perspective, our approach is comparable to the technique used within the Vorticity Transport Model [38] (even though the latter has no drag component), or to the Actuator Line Method. However, in those methods, the additional source terms originating at the line are regularized over several grid points and treated in a Eulerian fashion, thus constraining the allowable time step. That is precisely what the present treatment aims to avoid, by working on the vorticity instead. We explicitly identify and describe the bound vorticity which remains attached to the device, and the shed vorticity due to both lift and drag.

Notice that none of the above mentioned numerical models (including the present ILDL) are meant to provide a detailed representation of the flow around an actual device; their objective is to introduce the correct signature of the device in the wake.

3.1 Lift and drag evaluations

Under the assumption of a high aspect ratio device (such as a blade or a wing), the flow around each airfoil (i.e. each device section) is assumed essentially two-dimensional. We divide the device into spanwise elements of size Δz equal to the mesh size h. The i^{th} element runs between $[\mathbf{x}_{b_i}, \mathbf{x}_{b_{i+1}}]$, see Fig. 1. On that element, we define the sectional lift and drag as $\mathbf{L_{2D}}_i = L_{2D_i}\,\hat{\mathbf{e}}_\mathbf{L}$ and $\mathbf{D_{2D}}_i = D_{2D_i}\,\hat{\mathbf{e}}_\mathbf{D}$, and the circulation as $\boldsymbol{\Gamma}_i = \Gamma_i \hat{\mathbf{e}}_{\boldsymbol{\Gamma}}$. We also define the local velocity $\mathbf{u}_{0_i}$: the velocity "as measured on the line element". Then, $\mathbf{U}_{0_i}$ is the projection of that velocity on the sectional plane (by convention, we note the velocities in the sectional plane using an uppercase character). Finally, we define the "local effective upstream velocity", $\mathbf{U}_{e_i}$, i.e. the velocity used in the usual definition of the airfoil aerodynamic coefficients,

$$L_{2D_i} = \frac{1}{2}\rho\, U_{e_i}^2\, c_i\, C_l(\alpha_i, Re_i), \tag{5}$$

$$D_{2D_i} = \frac{1}{2}\rho\, U_{e_i}^2\, c_i\, C_d(\alpha_i, Re_i), \tag{6}$$

where c_i is the chord of the local airfoil and ρ is the fluid density. The lift and drag coefficients C_l, C_d are retrieved from tabulated polar data, using the local effective angle of attack α_i as defined in Fig. 1, and Reynolds number Re_i. It will be clearer in what follows that $\mathbf{U}_{0_i} \neq \mathbf{U}_{e_i}$ when the model accounts for parasitic drag. For the rest of this work, the index i will be omitted for the sake of lighter notation.

In classical lifting line methods, the airfoil is modelled as the section of a bound vortex of local circulation Γ. The bound vortex line runs through the aerodynamic center of each airfoil. In order to add the contribution of the parasitic drag, the model is here enhanced using two trailing vortex sheets (see Fig. 2a) which mimic a wake with a velocity deficit. These vortex sheets, of circulation per unit length γ and $-\gamma$ respectively, correspond to what is shed by a momentum sink located on the airfoil, or equivalently a vorticity dipole source. The spacing between the shed vortex sheets is d, and the dipole strength is $\mu = \gamma d$. Assuming small drag, we will here consider that the vortex sheets remain essentially parallel to each other in the near wake. In reality, the dipole sheets undergo a small expansion, becoming more important when the drag increases.

The dipole width d is a parameter of the model. Ideally, it should scale with the thickness of the device; the grid size h will however most often not allow to choose such small values. Still, the correct drag can be achieved using a larger d, as long as γ is set appropriately to $\gamma = \frac{\mu}{d}$.

The closure of the model necessitates relations between the aerodynamic forces, and the quantities Γ, μ. On the one hand, we use the Kutta-Joukowski theorem, as in [32], to relate the circulation to the sectional lift,

$$\mathbf{L_{2D}}(t) = \rho\,\mathbf{U}_0(t) \wedge \boldsymbol{\Gamma}(t)\ . \tag{7}$$

On the other hand, the sectional drag force is equal to the flux of momentum imparted to the flow by the vortex dipole source,

$$D_{2D}(t) = \rho\, U_0(t)\, \mu(t). \tag{8}$$

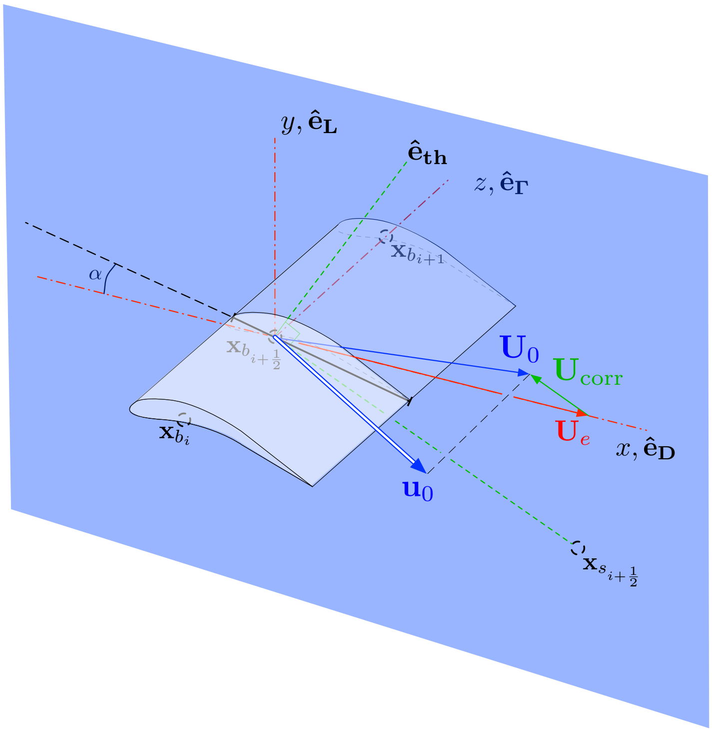

Fig. 1: Reference frame and velocities for the i^{th} element of the line.

The latter equation is subject to a small error due to the small expansion of the dipole sheets, as will be discussed in Section 4 and Appendix B.

Quasi-steadiness was assumed in Eqs. (7) and (8), and also in the polar data, as used in Eqs. (5) and (6). The developed model will thus be limited to aerodynamics with moderate unsteadiness. We note that a dynamic stall model could be used to replace the static polar data, and account for highly unsteady effects, as in [7,6,2].

Finally, combining resp. Eq. (5) with Eq. (7), and Eq. (6) with Eq. (8), we obtain the expressions of the circulation and of the dipole strength

$$\Gamma = \frac{1}{2}\frac{U_e^2}{U_0}\, c\, C_l \ , \tag{9}$$

$$\mu = \frac{1}{2}\frac{U_e^2}{U_0}\, c\, C_d \ . \tag{10}$$

To summarize, at each time step of the numerical method and for every element of the ILDL, one first obtains the local velocities. The techniques employed for the measurement of $\mathbf{U}_0$ and for the deduction of $\mathbf{U}_e$ are discussed hereafter. Then, from the determination of the corresponding angles (as shown in Fig. 2b) and of Re, the aerodynamic coefficients are retrieved from a look-up in the polar data. Eventually, Eqs. (9) and (10) yield the circulation and the dipole strength.

3.2 Measurement of the local velocity $\mathbf{U}_0$

The local velocity measurement has to account for the mollification of the vorticity. Indeed, as suggested by [9], Eq. (7) holds provided that the proper velocity is considered.

It is shown by [3] that the most consistent evaluation of the velocity on the lifting line consists in evaluating its “principal value”, obtained by integration of the velocity over the mollification region, in order to comply with the mollified formulation of the lifting line. This so-called “integral velocity

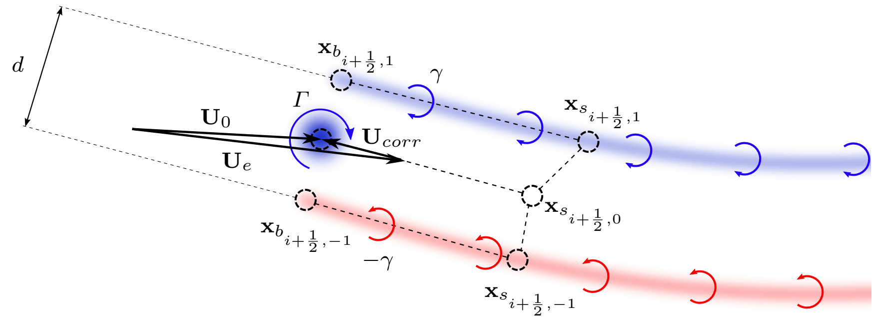

(a) ILDL with a bound vortex at the quarter chord, and two shed vortex sheets. The correction velocity $\mathbf{U}_{\text{corr}}$ is aligned with the shedding direction, obtained using tracers $\mathbf{x}_s$.

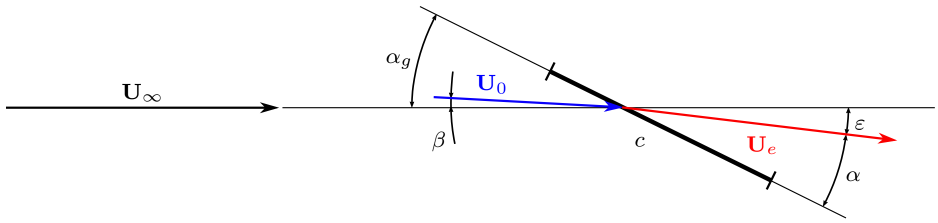

(b) In a steady uniform flow, a reference direction is given by the upstream flow velocity $\mathbf{U}_\infty$. Then, for each section of the device, we define the geometric angle of attack α_g with respect to the airfoil chord; the downwash angle ε and the local effective angle of attack $\alpha = \alpha_g - \varepsilon$, using the local effective upstream velocity $\mathbf{U}_e$; and the angle β between the local measured velocity and the reference direction.

Fig. 2: Schematic 2-D view of the lifting and dragging line model in steady conditions, and definitions of the characteristic angles.

sampling" is here implemented using the position of the bound vortex particles $\mathbf{x}_b$,

$$\mathbf{U}_{0_i} = \sum_j w_j \, \mathbf{U}(\mathbf{x}_{b_{i,j}}), \tag{11}$$

where $\mathbf{U}$ is the velocity field projected in the sectional plane. This is a marked departure from the popular choice within the ALM, which consists in the simple evaluation of $\mathbf{U}$ at the center of the bound vortex (i.e., a "pointwise sampling", $\mathbf{U}_{0_i} = \mathbf{U}(\mathbf{x}_{b_{i,0}})$), used e.g. in [39,20,25,26,27].

3.3 Reconstruction of the effective upstream velocity $\mathbf{U}_e$

In the absence of parasitic drag, we have that $\mathbf{U}_e = \mathbf{U}_0$ because the principal value of the velocity induced by the bound vorticity is zero. However, precisely because of the velocity induced by the dipole vortex sheets due to the drag, $\mathbf{U}_e$ will differ from $\mathbf{U}_0$. While the latter can be measured using Eq. (11), the effective upstream velocity $\mathbf{U}_e$ must be computed from $\mathbf{U}_0$ by injecting the theoretical dipole-induced velocity. The model for the recovery of $\mathbf{U}_e$ is provided in Appendix A. A similar procedure was proposed by [25] and [29] for actuator methods.

In practice, as depicted in Fig. 2, we use a vector correction, defining $\mathbf{U}_{\text{corr}}$, based on Eq. (24) and applied to the bound vortex particles,

$$\mathbf{U}_{e_i} = \mathbf{U}_{0_i} - \mathbf{U}_{\text{corr}_i} = \sum_j w_j \left(\mathbf{U}(\mathbf{x}_{b_{i,j}}) - \mathbf{U}^d_\sigma(\mathbf{x}_{b_{i,j}}) \right). \tag{12}$$

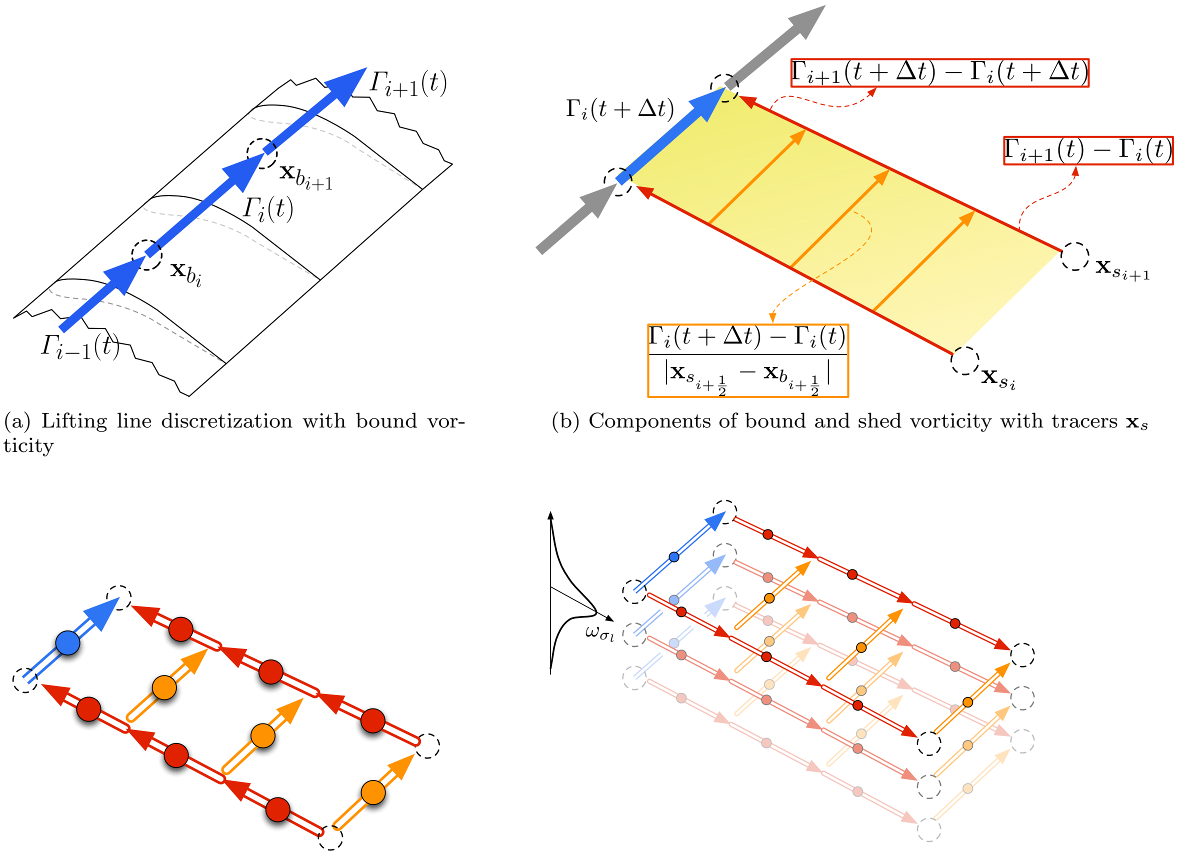

(a) Lifting line discretization with bound vorticity

(b) Components of bound and shed vorticity with tracers $\mathbf{x}_s$

(c) Particle discretization of bound and shed vorticity using one layer

(d) Discretizeation of bound and shed vorticity with mollification across the thickness, using multiple layers

Fig. 3: Discretization of a device and its wake using vortex particles (lift contribution only).

3.4 Bound vorticity, shed vorticity and Lagrangian treatment

The key aspects of the Lagrangian treatment of the bound and shed vorticity are depicted in Figs. 3 and 4. These vorticities are computed and updated over the course of a time step, based upon the evaluation of Eqs. (9) and (10).

Regarding the lift, the bound vorticity corresponds to $\Gamma_i(t)$, Fig. 3a. The shed vorticity has two components, Fig. 3b. The first one is due to the spanwise gradient of circulation and is aligned along the segment $[\mathbf{x}_{b_{i+1}}, \mathbf{x}_{s_{i+1}}]$ (an approximation of the streakline released over the time step). It has a strength, $\Gamma_{i+1} - \Gamma_i$, which depends on its release time, because of the time variation of the bound vorticity. That structure needs to be complemented with a sheet of uniform transversal vorticity, and of circulation per unit length equal to $\frac{1}{|\mathbf{x}_{s_{i+\frac{1}{2}}} - \mathbf{x}_{b_{i+\frac{1}{2}}}|}(\Gamma_i(t+\Delta t) - \Gamma_i(t))$: this ensures the solenoidal property on the combined shed structures.

Regarding the drag, spanwise gradients of the vorticity in the two vortex sheets (Fig. 4a) will exist due to the spatial variation of μ along the line, and it is hence required to close the vorticity loops with vortex sheets normal to the main sheets, see Fig. 4b.

The spatial arrangement of the shed vorticities in the near wake proceeds in a fashion similar to the Unsteady Vortex Lattice Method [22, Section 13.12] but here accounts for a non-zero thickness of the vortical structures. The bound vorticity and shed vortex sheets are indeed discretized by means of particles, Figs. 3c and 4c. Recall that these vortex particles will be interpolated on the grid when one needs to evaluate the grid based operations in the VPM solver. Therefore, in order to limit the effect of

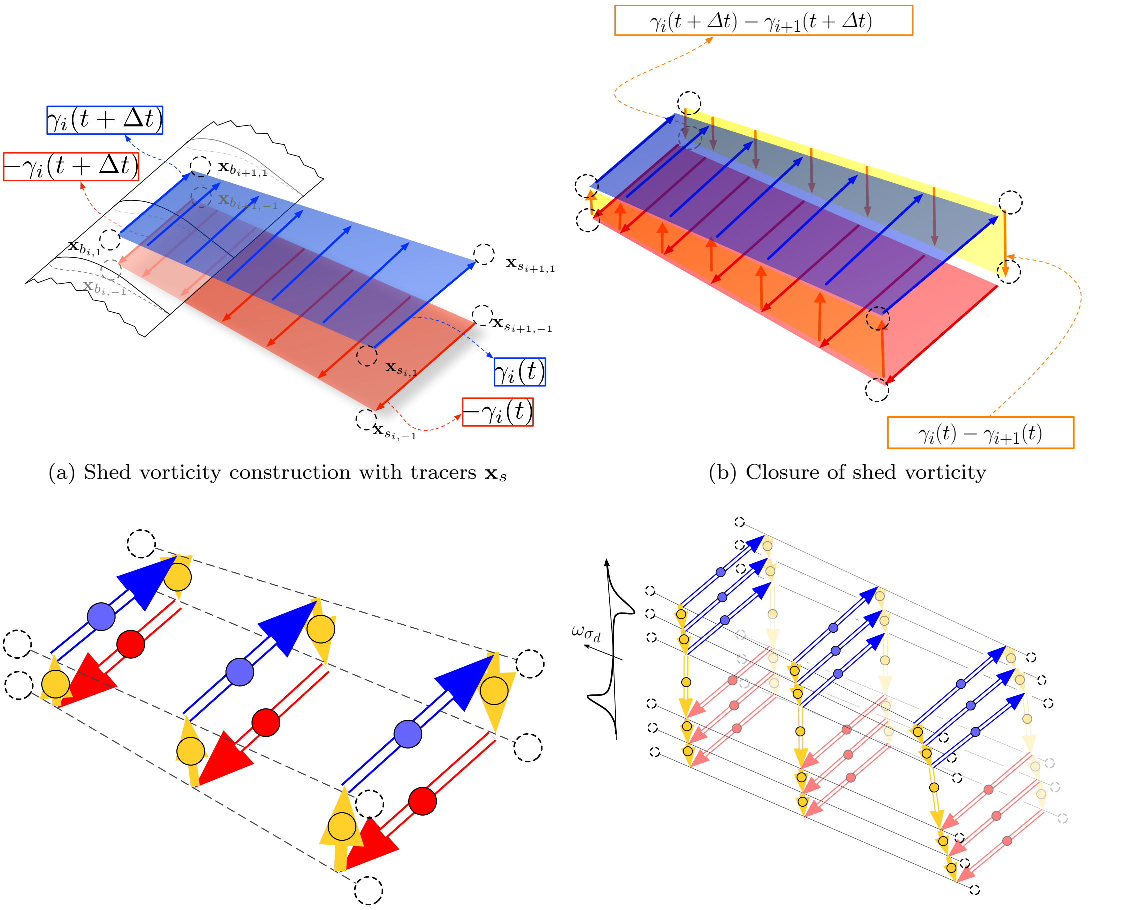

(a) Shed vorticity construction with tracers $\mathbf{x}_s$

(b) Closure of shed vorticity

(c) Particle discretization of shed vorticity

(d) Discretization of shed vorticity with mollification, using multiple layers

Fig. 4: Discretization of a device and its wake using vortex particles (drag contribution only).

the negative lobes of the high order interpolant $M'4$, a 1-D mollification is explicitly introduced in the thickness direction $\hat{\mathbf{e}}_{\mathbf{th}}$ by using several layers of particles. Each layer j accounts for a fraction of the vorticity, with a weight contributing to a partition of unity, see Figs. 3d and 4d. In practice, different mollification parameters can be used for the lift-induced vorticity, σ_l, and for the drag-induced vorticity, σ_d. The weights used per layer, w_j, are reported in Table 1 as a function of $\frac{\sigma}{h}$.

j	-4	-3	-2	-1	0	1	2	3	4
$\frac{\sigma}{h}=1$			0.010	0.208	0.564	0.208	0.010		
$\frac{\sigma}{h}=2$	0.005	0.030	0.104	0.220	0.282	0.220	0.104	0.030	0.005

Table 1: Weight per layer of particles w_j used for the 1-D Gaussian mollification.

To guide the layout of all the particles, several flow tracers $\mathbf{x}_{s_{i,j}}$ are initialized at the origin of each layer j ($\mathbf{x}_{b_{i,j}}$) and are advected by the flow over the course of the time step. These tracers allow the construction of a 3-D lattice over which the shed particles are distributed.

Advantageously, this geometrical construction is recomputed whenever it is needed during a substep of the time step, based on the updated position of the tracers. It therefore provides a proper representation of the current layout of the bound and shed vorticity. At the end of the time step, the shed vorticity is added to the bulk vorticity through a particle-to-particle interpolation (also using $M'4$), and the tracers are re-initialized for the next time step.

4 Validation of the Lifting and Dragging Line model

The VPM method with the ILDL is employed to simulate benchmark airfoils and wings, and the output quantities are compared to theoretical references. A list of the test cases considered in the rest of this section is presented in Table 2. The simulation results presented in this section were all obtained using a CFL number of $\frac{U_\infty \Delta t}{h} = 1$.

As a validation step, we check for the consistency of the model by verifying that the bound and shed vorticity actually corresponds to the force evaluated by the ILDL at all times. To this end, the forces applied on the fluid are measured by means of a control volume (CV) analysis, and compared to the performance of the ILDL, itself obtained from the integration of Eqs. (5) and (6). Formulas by [31] are used to compute the resultant force using a CV (Ω), based on the vorticity and velocity fields,

$$\begin{aligned}\frac{\mathbf{F}}{\rho} = &- \frac{1}{\mathcal{N}-1}\frac{d}{dt}\int_{\Omega} \mathbf{x} \wedge \boldsymbol{\omega}\, d\mathbf{x} + \int_{\Omega} \mathbf{u} \wedge \boldsymbol{\omega}\, d\mathbf{x} \\ &- \frac{1}{\mathcal{N}-1}\oint_{\partial\Omega} \left[(\mathbf{x}\wedge\boldsymbol{\omega})(\mathbf{u}\cdot\hat{\mathbf{n}}) - (\mathbf{x}\wedge\mathbf{u})(\boldsymbol{\omega}\cdot\hat{\mathbf{n}})\right] d\mathbf{x} \\ &+ \frac{1}{\mathcal{N}-1}\oint_{\partial\Omega} \mathbf{x} \wedge \left[\hat{\mathbf{n}} \wedge (\nabla\cdot\mathbf{T})\right] d\mathbf{x} + \oint_{\partial\Omega} \hat{\mathbf{n}}\cdot\mathbf{T}\, d\mathbf{x},\end{aligned} \tag{13}$$

where $\mathcal{N}$ is the number of dimensions (2 for airfoils or 3 for wings) and $\mathbf{T}$ is the sum of the viscous stress tensor and the SGS stress tensor.

From a numerical perspective, it is worth noticing that the forces computed using Eq. (13) are prone to oscillations coming from the discretization of the time derivative. In addition, the signatures of the remeshing and the reprojection operations, which are necessary steps in the VPM method, will sometimes be visible on the time evolution of $\mathbf{F}$. Therefore, when we present the steady state force measurement hereunder, these are averaged over one reprojection period.

4.1 Airfoils

A first set of simulations is performed using the VPM method, with periodic boundary conditions in the spanwise direction, thus simulating an airfoil section over a short spanwise extent. The line is placed at the center of a computational domain of length $256h$ in the streamwise direction, and of height $128h$. The chord c of the airfoil is such that $\frac{c}{h} = 4$.

Concerning the airfoil polar, the lift slope is generally assumed equal to 2π, and the drag coefficient is supposed constant. The polar used in each case is also shown in Table 2.

Case	Chord distribution	AR	airfoil polars	
Airfoil A			$C_l = 2\pi\,\alpha$	$C_d = 0.0$
Airfoil B			$C_l = 0.0$	$C_d = 0.1$
Airfoil C			$C_l = 2\pi\,\alpha$	$C_d = 0.1$
Wing D	elliptical	10	$C_l = 2\pi\,\alpha$	$C_d = 0.0$
Wing E	elliptical	10	$C_l = 2\pi\,\alpha$	$C_d = 0.1$
Wing F	retangular	10	$C_l = 2\pi\,\alpha$	$C_d = 0.1$
Wing G	linearly tapered	10	$C_l = 2\pi\,\alpha$	$C_d = 0.1$
Wing H	elliptical	10	$C_l = 2\pi\,\alpha$	$C_d = 0.025$

Table 2: List of 2-D airfoils and 3-D wings under study. The Wing G is twisted so as to produce a bell-shaped circulation distribution when $C_L = 1$.

	σ_l/h	ε	$Err(C_l)$ [%]		$C_d/C_l^{th} \times 10^2$	
			ILDL	CV	ILDL	CV
(a)	1	0.15°	-1.53	-1.53	0.26	0.26
(b)	2	0.14°	-1.36	-1.37	0.24	0.24
(c)	1	0.08°	-0.80	-0.80	0.14	0.14

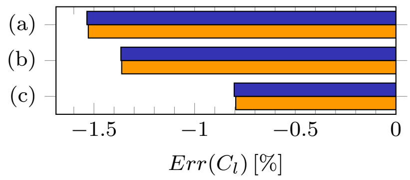

Table 3: Error on the steady state lift, $Err(C_l) = \frac{C_l - C_l^{th}}{C_l^{th}}$, and drag coefficients developed by the ILDL on Airfoil A, as evaluated by the ILDL model (orange) and as measured by the CV analysis (blue). Case (c) was obtained using a domain twice longer.

4.1.1 Airfoil with lift only

First, we consider Airfoil A which models a purely lifting airfoil, at a geometric angle of attack (AoA) of $\alpha_g = \alpha_1$, such that $C_l^{th}(\alpha_1) = 2\pi\alpha_1 = 1.0$. The lift and drag coefficients obtained in steady state (Table 3) are compared to their theoretical counterparts.

Cases (a) and (b) explore the influence of the mollification on the ILDL, with ratios $\frac{\sigma_l}{h}$ taken as 1 and 2 respectively. While an almost perfect agreement is reached between the ILDL and the CV evaluations, a small discrepancy is observed with respect to the theoretical values. It is here due to the symmetries imposed by the inflow/outflow boundary conditions implemented in the Poisson solver for Eq. (2) (as explained in Appendix C.): the "image vorticity field" induces a small spurious downwash velocity on the line, thus reducing the AoA and tilting the lift vector by an angle ε, which also explains the occurence of a small drag. We verify, with case (c), that the errors are indeed reduced by a factor of 2 when the domain size is doubled in the streamwise direction.

4.1.2 Airfoil with parasitic drag only

Tests of the ILDL are then performed on Airfoil B which has no lift and $C_d^{th} = 0.1$. Even though this value is one order of magnitude higher than the typical value of C_d for an airfoil at moderate AoA, our drag model is still valid, as shown by the following results. We also assess the accuracy of the effective upstream velocity reconstruction method, Eq. (12), for which we verify that $\frac{C_d^{th} c}{d}$ is indeed at most equal to 0.1, as required (see Appendix A.).

The results with a contant ratio $\frac{\sigma_d}{h} = 1$ and increasing d are presented in Table 4. The effect of the mollification is also tested with case (g), using $\frac{\sigma_d}{h} = 2$.

A small error is observed between the drag evaluated on the ILDL and the actual drag measured using the CV. This error comes from the small expansion of the dipole, which is not accounted for in Eq. (8). As verified by the evaluation (not shown here) of each term in Eq. (13), the main contribution to the drag is due to $\int_{\partial\Omega} (\mathbf{x} \wedge \boldsymbol{\omega})(\mathbf{u} \cdot \hat{\mathbf{n}})\, dS$ which is directly related to Eq. (8). Yet, a small contribution is brought by $\int_{\Omega} (\mathbf{u} \wedge \boldsymbol{\omega})\, d\Omega$, due to the curvature and the mollification of the vortex sheets. For the singular case considered in Appendix B.1, the latter integral scales as $-\frac{\mu\gamma}{2}$. The drag force actually injected in

	$\frac{\sigma_d}{h}$	$\frac{d}{h}$	$\frac{U_0}{U_\infty}$	$\frac{U_e}{U_\infty}$	$Err(C_d)$ [%]	
					ILDL	CV
(d)	1	4	0.97	1.00	-0.83	-1.93
(e)	1	6	0.98	1.00	-0.42	-1.18
(f)	1	10	0.99	1.00	-0.20	-0.31
(g)	2	10	0.99	1.00	-0.16	-0.65

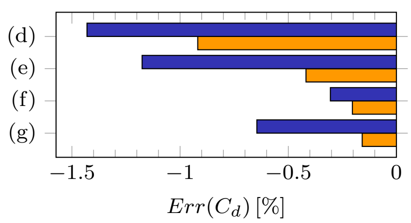

Table 4: Steady state drag coefficients developed by the ILDL on Airfoil B, as evaluated by the ILDL model (orange) and as measured by the CV analysis (blue), and numerical values of the corresponding error $Err(C_d) = \frac{C_d - C_d^{th}}{C_d^{th}}$. Local evaluation of the velocity U_0 and reconstructed effective upstream velocity U_e
.

	layout	$\frac{U_e}{U_\infty}$	ε	$Err(C_l)$ [%]		$Err(C_d)$[%]	
				ILDL	CV	ILDL	CV
(h)	I	0.99	0.03°	-2.95	-5.01	-0.81	-5.12
(i)	II	0.99	0.17°	-3.76	-5.61	1.87	-0.99
(j)	III	1.00	0.21°	-2.64	-3.65	3.34	2.30

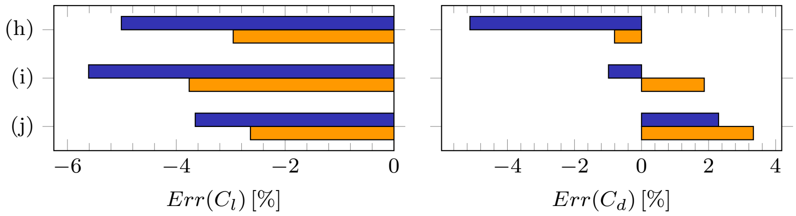

Table 5: Steady state lift and drag coefficients developed by the ILDL on Airfoil C, as evaluated by the ILDL model (▬) and as measured by the CV analysis (▬). Performance of the effective upstream velocity reconstruction, in terms of norm and downwash angle.

the flow is therefore slightly smaller than that computed by the ILDL. It is also slightly affected by the mollification factor as demonstrated by case (g).

The remaining discrepancy between the ILDL evaluation and the theoretical value of C_d^{th} can be explained by the error on the upstream velocity reconstruction. As d/h increases with constant μ, the circulation per unit length γ decreases and we observe that $\frac{U_e}{U_\infty} \longrightarrow 1$. Overall, the relative error on the drag remains below 1.5%.

4.1.3 Airfoil with lift and parasitic drag

We finally consider Airfoil C which produces lift and drag. In that case, the upstream velocity reconstruction should ideally yield a velocity vector $\mathbf{U}_e$ close to that observed on Airfoil A (i.e. without drag).

Various combinations of $\frac{\sigma_l}{h}$, $\frac{\sigma_d}{h}$ and $\frac{d}{h}$ are chosen such that different levels of compactness of the line discretization are achieved. The respective layouts of the particles in the thickness are presented in Fig. 5, and yield a total height of 5, 9 and 11 particles. The corresponding simulations results are shown in Table 5.

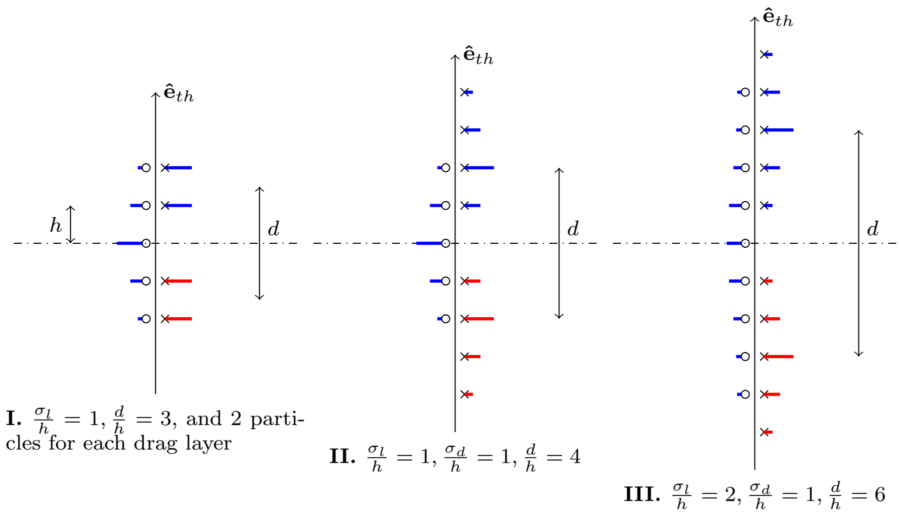

Fig. 5: Three possible layouts of the particle layers in the thickness of the ILDL, with lift particles (∘), and drag particles (×). The color bars represent the weight.

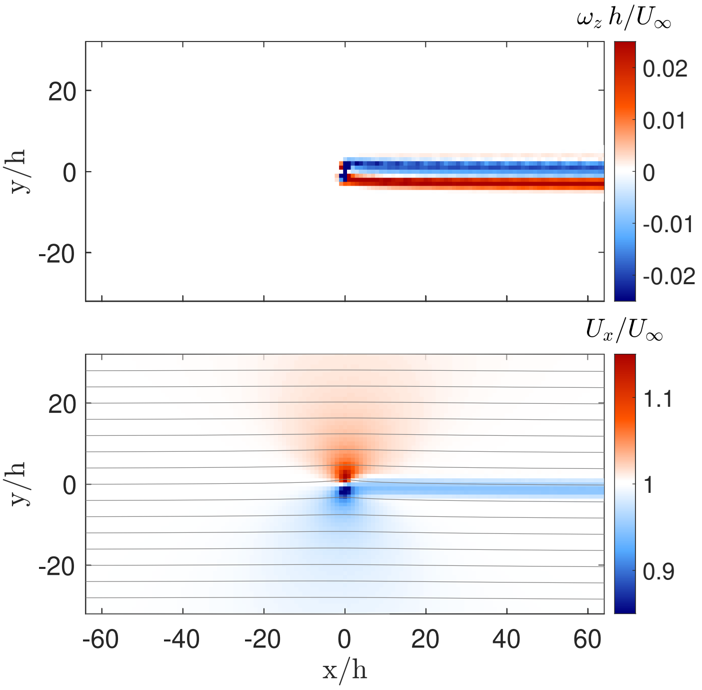

Fig. 6: Spanwise vorticity ω_z and streamwise velocity U_x in case (i), with an acceleration above the airfoil and a deceleration below, due to the bound vortex.

The magnitude of the effective upstream velocity is recovered within 1% error. The small spurious downwash angle (which must be compared to the ε values of Table 3) depends on the particle layout. As a result, in comparison with the theoretical values, the lift coefficient is reduced because of the slightly smaller effective AoA, and the drag is increased because the lift vector is slightly tilted backward.

The measurements using the CV and the evaluation by the ILDL also show a slight disagreement. This is attributed to a combination of several effects. First, as explained in the previous section, the curvature of the dipole sheets results in a smaller drag measured using the CV. Second, the ILDL models lift and drag as if they were purely additive. In fact, the combination of those two leads to the occurence of some “drag-induced lift” which originates in the loss of symmetry in the streamwise velocity field and its interaction with the drag-induced vorticity (as observed in Fig. 6). This interaction produces a lift force that scales as $-\frac{\Gamma\gamma}{2}$ for the singular case, as shown in B.2.

In our simulations, the use of the most compact particle layout I leads to the largest inconsistency, with 2% difference between the ILDL and CV evaluations of the lift, and 4% for those of the drag. Still, these levels remain quite acceptable, given the simplicity of the model. Besides, the asymmetry is reduced with the increase of σ_l/h and σ_d/h, and so is the difference between the CV and ILDL evaluations. We conclude that the ILDL model, together with its implementation in VPM, yield fairly accurate results in such 2-D simulations.

4.2 Wings

The focus is now set on wings of span b, without sweep or dihedral. They are placed at the center of a computational domain of length $4b$ in the streamwise direction, and $2b$ in both of the transverse unbounded directions.

Wings D and E are elliptical untwisted wings. Wing F is a rectangular untwisted wing. Wing G is designed to produce a “bell-shaped” circulation distribution [43], which exhibits a zero slope at the tip, as opposed to the elliptical and rectangular wings. It is linearly tapered (with a ratio between the root chord and the tip chord of $\frac{1}{2}$) and it has a twist distribution computed such that the desired circulation distribution is obtained at the design AoA (here equal to $C_L = 1$).

Again, the evaluations of the global lift and drag coefficients based on the ILDL and on the CV approaches will be compared. In addition, the induced velocities, circulation distributions, and lift and drag coefficients will be compared to results from the classical Prandtl Lifting Line (PLL) theory, and to those from the mollified PLL theory [3], recalled in the next section. Indeed, the mollified PLL provides analytical results which account for the mollification, and hence constitutes a better theoretical reference for the ILDL than its singular counterpart, for a given value of the mollification parameter σ. We also notice that the mollified PLL converges to the singular PLL when $\sigma \to 0$. Still, discrepancies between the mollified reference and the ILDL model may exist, on the one hand due to the absence of parasitic drag and to the prescription of the wake geometry (i.e. the shed vortex sheet does not roll up) in the PLL theory, and on the other hand, due to numerical errors in the ILDL.

4.2.1 Reference lifting line with mollification

The classical lifting line theory by [34] relates the circulation distribution $\Gamma(z)$ over a slender lifting surface to the effective angle of attack $\alpha(z) = \alpha_g(z) - \varepsilon(z)$ (see Fig. 2b), where the downwash angle ε is itself a function of the circulation distribution. Prandtl's compatibility equation reads

$$\Gamma(z) = \frac{1}{2} a_0 \, c(z) \, U_\infty \left(\alpha_g(z) - \varepsilon(z)\right), \tag{14}$$

where ε is deduced from the Biot-Savart law which provides the velocity induced by the wake on the lifting line.

In the original theory, the line itself and the wake vortex sheet are singular, leading to a singular vorticity field $\boldsymbol{\omega}_\delta(\mathbf{x})$. The downwash angle on the line is thus

$$\varepsilon(z) = \frac{1}{U_\infty} \frac{1}{4\pi} \int_{-b/2}^{b/2} \frac{1}{(z - z')} \frac{d\Gamma}{dz'} \, dz'. \tag{15}$$

The mollified lifting line, as proposed in [3], considers the regularized versions of these fields. Given a regularization function $\xi_\sigma(\mathbf{x})$ where σ is a smoothing parameter, the mollified vorticity field is defined as the convolution $\boldsymbol{\omega}_\sigma(\mathbf{x}) = \xi_\sigma(\mathbf{x}) * \boldsymbol{\omega}_\delta(\mathbf{x})$. The mollified velocity field $\mathbf{u}_\sigma(\mathbf{x})$ is obtained from the Biot-Savart law applied to $\boldsymbol{\omega}_\sigma$. In those conditions, Eq. (14) remains valid provided that the downwash is replaced by its mean (i.e. principal) value,

$$\Gamma(z) = \frac{1}{2} a_0 \, c(z) \, U_\infty \left(\alpha_g(z) - \bar{\varepsilon}_\sigma(z)\right), \tag{16}$$

where $\bar{\varepsilon}_\sigma(z) = -\frac{1}{U_\infty} \left[\xi_\sigma(\mathbf{x}) * (\mathbf{u}_\sigma(\mathbf{x}) \cdot \hat{\mathbf{e}}_y)\right]_{x=y=0}$ results from the so-called "integral velocity sampling".

Advantageously, the effects of the mollification can be highlighted using this mathematical framework, independently from any numerical method. As an example, the reference downwash and circulation distributions for Wings D to G are shown in Fig. 7, as a function of $\xi = -\frac{z}{b/2}$. Results are obtained using the singular PLL theory, and using the mollified PLL theory with uniform smoothing in span. Compared to the singular PLL, the mollified curves exhibit the same trend, except at the tip. Most notably, the 1-D mollification seems better suited than the 3-D mollification to reproduce tip behaviors similar those of the singular PLL. Especially at the tip of the rectangular wing, the 3-D mollified distribution is not monotonous, which leads to the shedding of undesired opposite sign vorticity in the wake. This is due to the additional spanwise smearing involved in the 3-D mollification.

Because it is based on mollification, the mollified PLL theory constitutes an attractive theoretical reference for the numerical methods with mollification. For instance, in the remainder of this study, the distributions obtained with the ILDL model will be compared to those predicted by the mollified PLL with a 1-D (vertical) Gaussian mollification kernel, $\xi_\sigma(\mathbf{x}) = \delta(x) \left(\frac{1}{\sqrt{\pi}\,\sigma} e^{-\frac{y^2}{\sigma^2}}\right) \delta(z)$. Similarly, it is worth mentioning that the ALM can also be compared to the mollified lifting line theory, when a 3-D mollification kernel is used (thus involving smoothing in x and z as well). For the latter, and in line with our comment on Fig. 7, it is shown in [3] and in [26] that the spanwise contribution to the mollification introduces a smearing of the $\Gamma(z)$ distribution and, consequently, of the forces on the line. This is precisely what the present ILDL method aims to avoid, and further motivates the choice of the 1-D mollification.

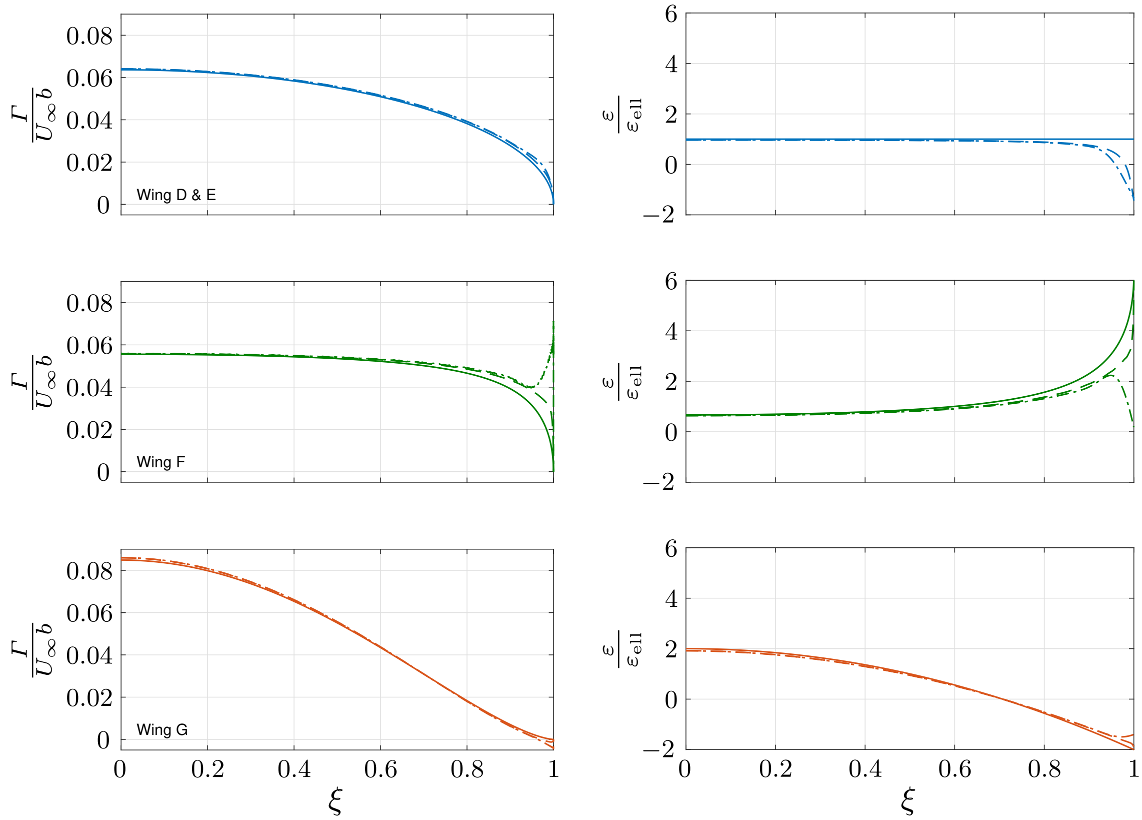

Fig. 7: Distributions of circulation and downwash angle when using the classical (singular) PLL at $C_L = 1$ (——); at the same AoA, when using the 1-D (vertical) mollified PLL (- - -), and the 3-D mollified PLL (-·-·-) with $\frac{\sigma}{b} = \frac{1.2}{64}$: Wing D or E (top), Wing F (center) and Wing G (bottom).

4.2.2 Wings with lift and induced drag

We now validate the ILDL model on an elliptical wing without parasitic drag (Wing D). The wing is not twisted: $\alpha_g(z) = \alpha_g$. We recall the theoretical results from the classical PLL (presented in Fig. 7): the downwash angle ε is uniform across the span and equal to $\varepsilon_{ell} = \frac{2}{(AR+2)}\alpha_g$. The circulation is elliptical, $\Gamma_{ell}(z) = \Gamma_0\sqrt{1-\xi^2}$ with $\Gamma_0 = \frac{2bU_\infty}{\pi AR} C_L^{th}$. The wing lift coefficient is $C_L^{th} = \frac{AR}{(AR+2)} 2\pi\alpha_g$, and the induced drag coefficient is $C_{D_i}^{th} = \varepsilon_{\mathrm{ell}} C_L^{th} = \frac{C_L^2}{\pi AR}$.

The steady state results are obtained at the end of simulations where the AoA is linearly varied from $\alpha_g = 0$ to $\alpha_g = \alpha_1$ in a time corresponding to $\tau = \frac{U_\infty T}{b} = 1$. The time evolution of the aerodynamic coefficients is depicted in Fig. 8. The force evaluation of the ILDL and the forces measured on the CV show good agreement, even during the transient, which illustrates the consistency of the approach. Notice the small amplitude oscillations on the CV evaluation, that is due to the reprojection step of the VPM method.

In order to further validate the approach, two parametric explorations, are performed. For the first one, the ratio σ_l/h is kept constant while increasing the spatial resolution, by reducing h/b. Table 6 shows that the lift and drag evaluations converge roughly at first order to the values predicted by the classical PLL, $C_L^{th}(\alpha_1) = 1$ and $C_D^{th}(\alpha_1) = 0.0318$. This is consistent with the typical behavior of penalization and actuator methods where a singular forcing term has to be mollified. Locally, the ILDL downwash distribution (Fig. 9a) exhibits smaller values than the uniform distribution ε_{ell}, which explains the slightly higher C_L and lower C_D; but the error decreases as the mesh is refined. The circulation distribution (Fig. 9b) reflects the same behavior with respect to the reference elliptical distribution Γ_{ell}, with a

	h/b	σ_l/h	$Err(C_L)$ [%]		$Err(C_D)$ [%]	
			ILDL	CV	ILDL	CV
(k)	1/32	1	3.02	3.18	-12.50	-16.03
(l)	1/64	1	1.69	1.46	-7.71	-6.74
(m)	1/128	1	0.67	0.92	-4.04	-7.73

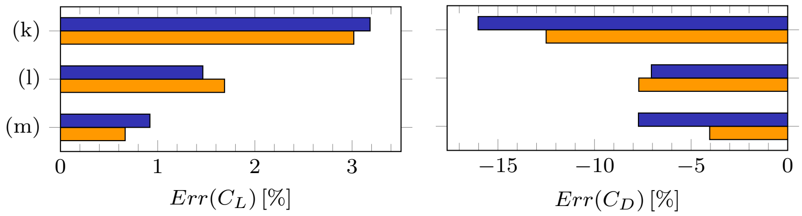

Table 6: Steady state lift and drag coefficients developed by the ILDL on Wing D, as evaluated by the model (orange) and as measured by the CV analysis (blue): parametric investigation with increasing resolution and with $\sigma_l/h = 1$. The errors are measured relatively to the classical PLL results (C_L^{th}, C_D^{th}).

maximum error at the tip. The difference never exceeds 6% though, and it rapidly decreases further from the tip. The maximum difference would be much larger if a spanwise mollification was also present in the method.

Notice that the 3-D effects here overcome the influence of the symmetry imposed through the inflow-outflow boundary condition, which was leading to a small error on the lift and drag coefficients in the 2-D simulations.

A close comparison of the coefficients recovered by the CV with those of the ILDL reveals small discrepancies, which here may be attributed to the shedding scheme described in Section 3. In fact, before they are released in the bulk flow, the shed particles follow a straight line to a tracer, and thus lack any curvature present in the actual streaklines. This local inconsistency introduces a perturbation on the lift and drag signatures of the ILDL in the flow. Still, the obtained coefficients are relatively close, which again confirms the consistency of the method.

For the second parametric study, the ratio σ_l/b is kept constant while the mesh is refined, therefore reproducing a mollified lifting line with increasing accuracy. We must here also account for the fact that the ILDL is subjected to an additional smoothing caused by the high order interpolation used in

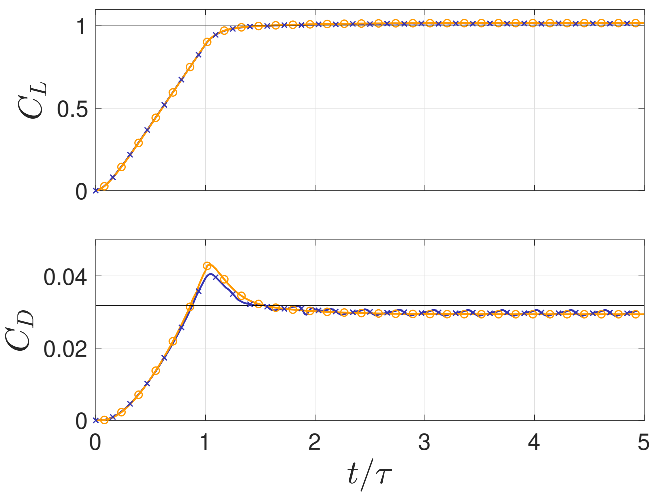

Fig. 8: Time evolution of the lift and drag coefficients developed by the ILDL on Wing D, case (l), as evaluated by the model (—o—) and as measured by the CV analysis (—×—). For comparison, the steady state values obtained using the classical PLL (——) are also displayed.

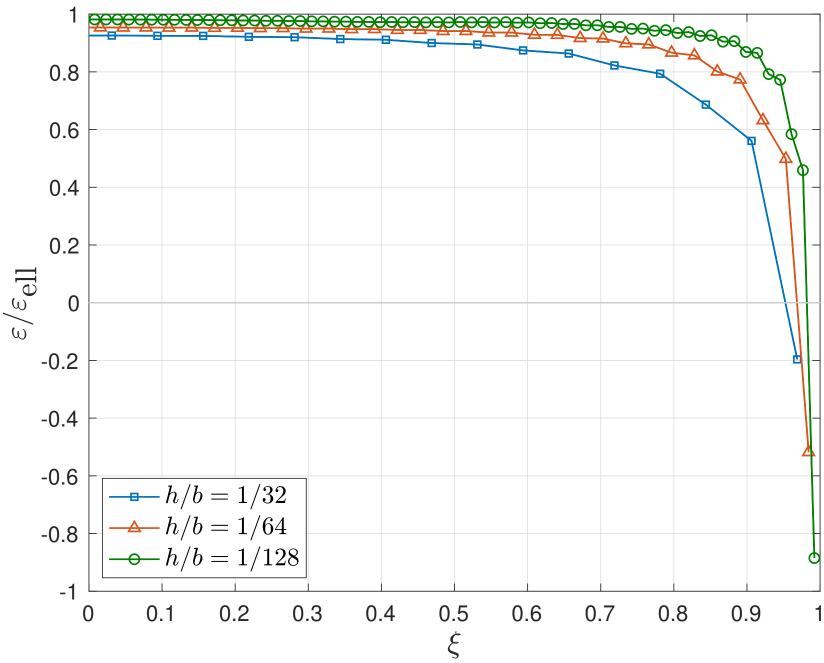

(a) Downwash distribution

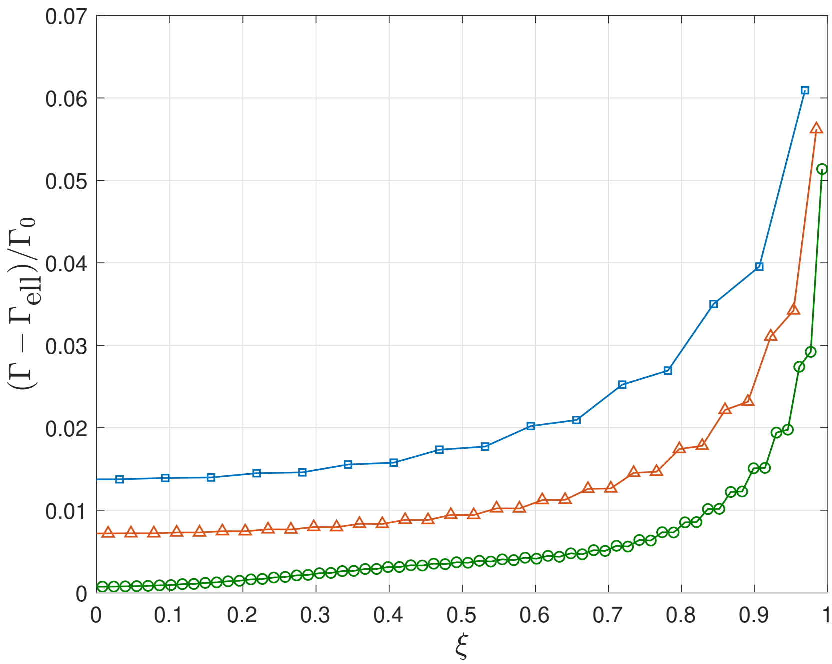

(b) Difference on the circulation distribution

Fig. 9: Results of ILDL for an elliptical wing without parasitic drag (Wing D) for three mesh resolutions and with constant $\sigma_l/h = 1$. The classical PLL prediction corresponds to an elliptical circulation distribution Γ_{ell} and a uniform downwash ε_{ell}.

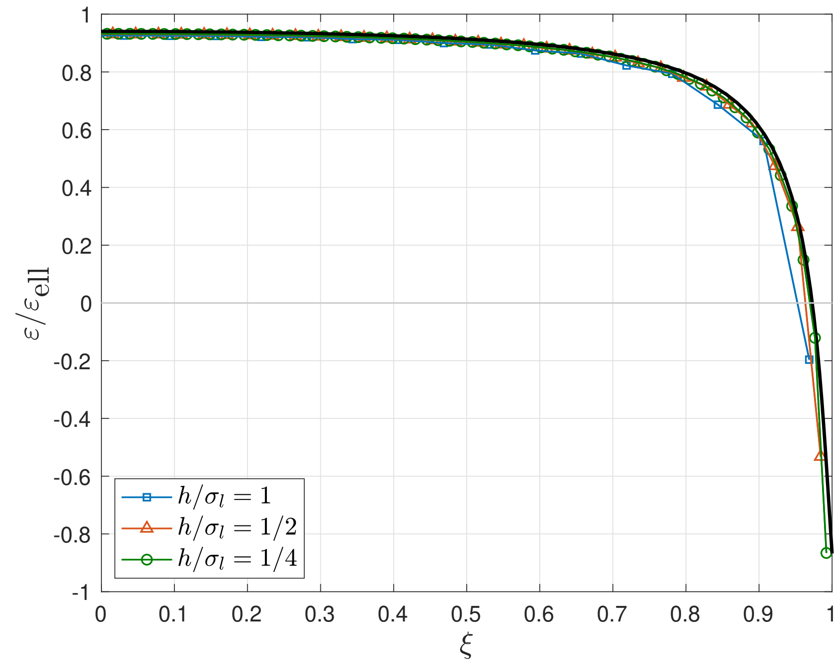

(a) Downwash distribution

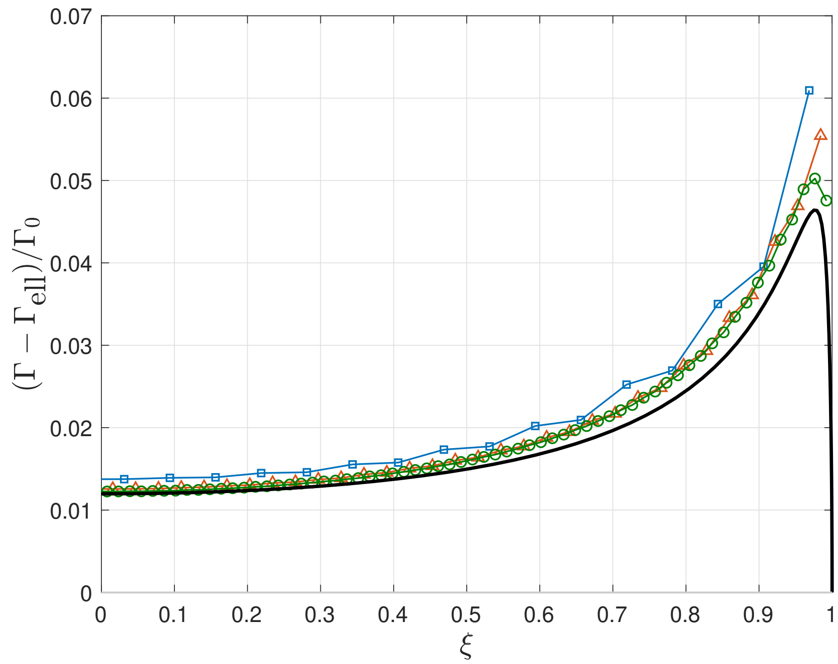

(b) Difference on the circulation distribution

Fig. 10: Results of ILDL for Wing D, for three mesh resolutions and with constant $\sigma_l/b = 1/32$. The mollified PLL results, using an effective smoothing of $1.2\sigma_l/b$, are also shown (▬).

	σ_l/b	h/σ_l	$Err(C_L)$ [%]		$Err(C_D)$ [%]	
			ILDL	CV	ILDL	CV
(n)	1/32	1	0.60	0.76	-2.46	-6.39
(o)	1/32	1/2	0.25	0.41	-1.49	-5.89
(p)	1/32	1/4	0.16	0.29	-1.25	-7.46

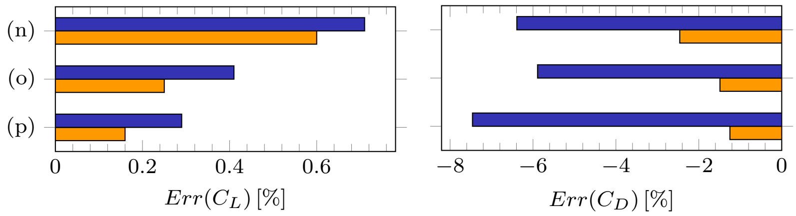

Table 7: Steady state lift and drag coefficients developed by the ILDL on Wing D, as evaluated by the model (orange) and as measured by the CV analysis (blue): parametric investigation with fixed mollification $\sigma_l/b = 1/32$ and with increasing resolution. The errors are measured relatively to the mollified PLL results [3], with an effective smoothing of $1.2\sigma_l/b$.

VPM. Indeed, the operation of transferring the shed particles generated on the lattice to the mesh entails an intrinsic smoothing of the vorticity, which depends on the orientation of the lattice with respect to the grid. Empirically, we found that using an effective smoothing factor increased by 20% leads to satisfactory agreement on the ILDL lift and drag coefficients (Table 7), as the theoretical mollified values, obtained after solving Eq. (16), are $C_{L_\sigma}^{th}(\alpha_1) = 1.024$ and $C_{D_\sigma}^{th}(\alpha_1) = 0.0285$. The same conclusion can be drawn from the circulation and downwash distributions (Fig. 10) at the root. The discrepancy further increases in the tip region where spanwise velocities cause a shear-like distortion in the shed particles. Indeed, the "suction side" particles move slightly inboard, while the "pressure side" ones, outboard. The resulting distorsion in the very-near-wake vorticity field contributes to a spanwise smearing of the induced velocities. Besides, we capture the Gaussian smoothing with few particles (five in this case), which leads to an additional error.

Overall, only small errors are produced, and the ILDL thus provides reliable results when there is no parasitic drag.

4.2.3 Wings with lift, induced drag and parasitic drag

The cases of Wings E, F and G are now considered; those combine lift, induced drag and parasitic drag. Their lift and total drag coefficients obtained with the ILDL method are shown in Table 8. The chosen $AR = 10$ is typical of aircraft wings, and corresponds to a mean aerodynamic chord $\bar{c} = \frac{S}{b}$ such that $\frac{h}{\bar{c}} = \frac{h}{b}\frac{b}{\bar{c}} = \frac{10}{64}$. This yields the ratio $\frac{\sigma_l}{\bar{c}} \simeq 0.16$, which can be compared to the smoothing factor of $\frac{\sigma_l^{\text{opt}}}{c} = 0.25$ proposed in [25], and obtained by comparison with 2-D blade resolved simulations. The accuracy of the ILDL method is thus expected to be similar to that of [25], likely with even sharper spanwise distributions (again coming from the absence of spanwise smoothing in that direction).

	Wing	h/b	layout	C_L			C_D		
				ILDL	CV	Δ	ILDL	CV	Δ
(q)	E	1/64	I	0.986	0.970	+0.016	0.1228	0.1157	+0.0071
(r)	F	1/64	I	0.994	0.981	+0.013	0.1212	0.1254	−0.0042
(s)	G	1/64	I	0.957	0.961	−0.004	0.1345	0.1294	+0.0051

Table 8: Steady state lift and drag coefficients developed by the ILDL on wings E, F and G, using $d/h = 3$, as evaluated by the ILDL model and as measured by the CV analysis.

As expected, small discrepancies are found between the aerodynamic coefficients estimated by the ILDL and those obtained from the CV analysis. All the previously mentioned factors explain their vari-

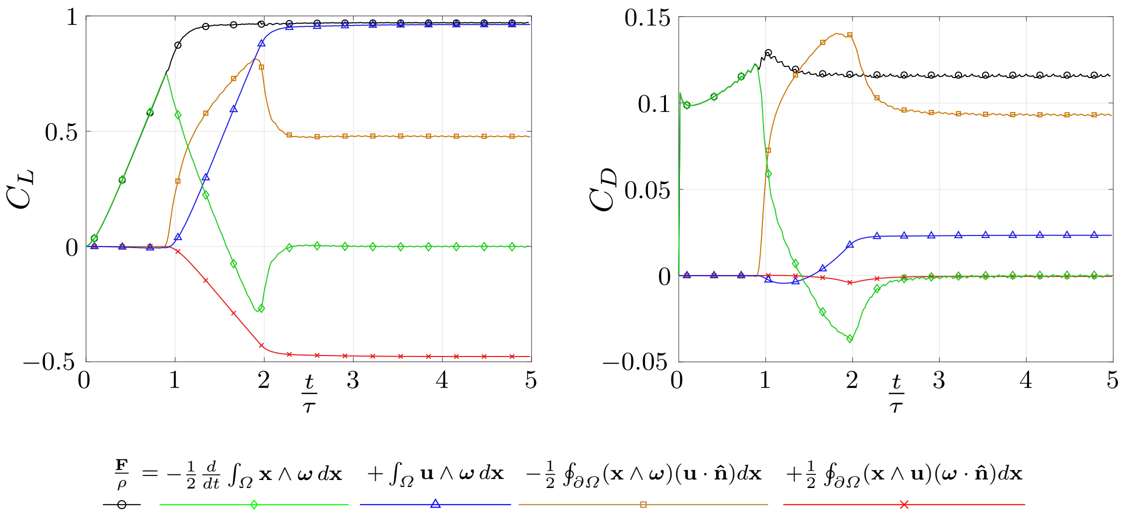

Fig. 11: Contributions to the lift and drag coefficients from the various terms in Eq. (13), in case (q). The terms involving $\mathbf{T}$ are here negligible.

ability across the three wings considered: the model error identified in Section 4.1.3, the error on the reconstructed upstream velocity, and the recourse to a particle lattice in the very near wake.

The contributions of the various terms in the CV analysis are shown in Fig. 11 for Wing E. Initially, the vorticity is contained in the CV and the force comes entirely from the time derivative term. In steady state, the lift is almost entirely recovered from the volume integral of $\mathbf{u}\wedge\boldsymbol{\omega}$, which is directly related to the Kutta-Joukowsky theorem. That term is also essentially associated with the induced drag. The two boundary terms are almost perfectly cancelling each other for the lift, whereas they appear to be related to the parasitic drag.

These last two comments are in line with the conclusions of [41], also noticing that the origin of each contribution to the force can't be clearly identified from a wake analysis. The final formula for $\mathbf{F}$ proposed in the same reference is compatible with the present control volume analysis when the steady state is reached, even though the last four terms of Eq. (13) corresponds to a single term of total pressure deficit in [41, eq.(2.45)].

Figure 12 assesses the quality of the recovered effective upstream velocity $\mathbf{U}_e$, in comparison with the theoretical one obtained using the mollified lifting line theory [3]: the downwash angle ε of the recovered $\mathbf{U}_e$ (Fig. 12a) is much closer to the theoretical angle than the angle β of the measured velocity $\mathbf{U}_0$. The same can be observed regarding the magnitude of $\mathbf{U}_e$ (Fig. 12b). From a measured velocity with a deficit of up to 10%, the upstream velocity is recovered well within 3% for all wings.

The circulation distribution is actually affected by the presence of the parasitic drag, as shown in Fig. 13a. However, it cannot be compared to the theoretical distribution as such. Indeed, Eq. (9) specifies that the local lift of a lifting line is proportional to $\frac{U_0}{U_e^2}\Gamma$, which is the only quantity that can be compared between wings of same lift, with and without parasitic drag. Therefore, the properly scaled distributions are presented in Fig. 13b, which shows that the ILDL successfully produces the expected distribution for the three wings considered, with only minor discrepancies in the tip region.

Additionally, we notice that the shape of the circulation distribution of the mollified results (mollified PLL and ILDL) near the tip differs significantly from that obtained using the classical PLL. The largest discrepancies are observed near the tip of the elliptical (E) and rectangular (F) wings, because of the infinite slope behavior of the circulation distribution at the tip (provided by the classical PLL). The differences are much attenuated for the bell-shaped wing (G), thanks to the zero slope at the tip.

Finally, it is verified that the difference between the lift and drag obtained by the two independent methods (CV and ILDL) indeed decreases when the absolute value of lift and drag are decreased. The Wing H is placed at an AoA four times smaller than all previous tests, and the corresponding airfoil

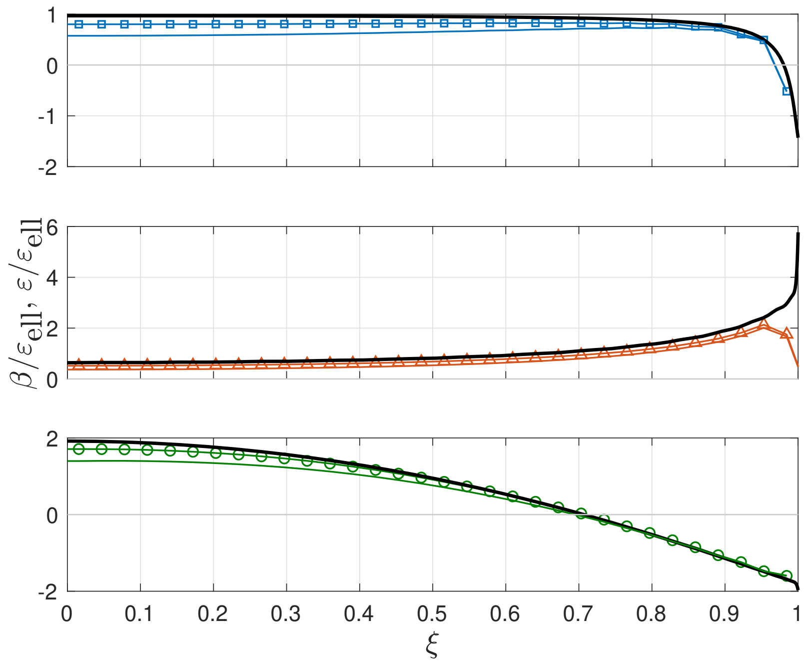

(a) Distribution of the measured velocity angle β (no symbol), and of the reconstructed downwash angle ε (symbol). The downwash angle as obtained using the 1-D mollified PLL with effective smoothing of $1.2\sigma_l/b$ is also presented (▬▬).

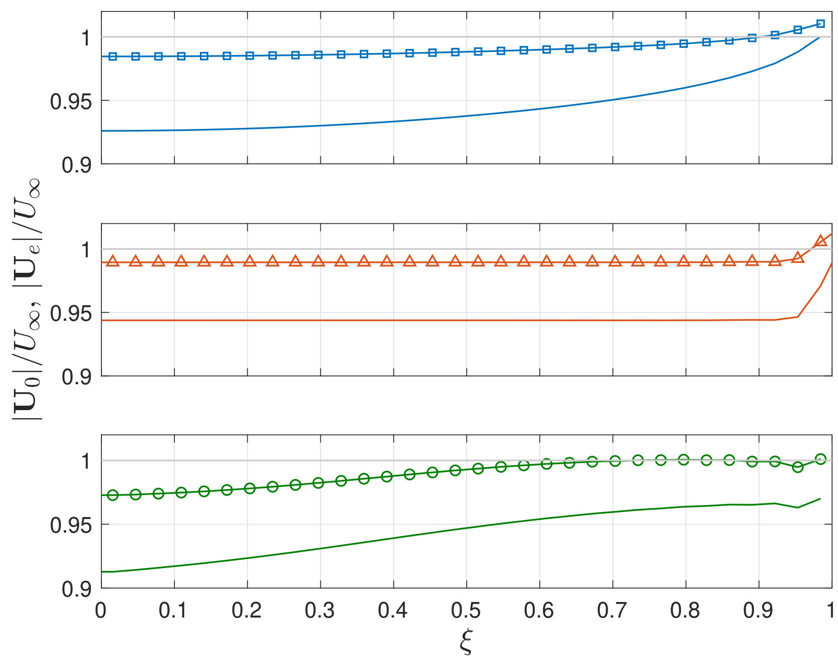

(b) Norm of the reconstructed effective upstream velocity $\mathbf{U}_e$ (symbol) and of the measured velocity $\mathbf{U}_0$ (no symbol)

Fig. 12: Performance of the effective upstream velocity reconstruction on Wing E (——), F (——) and G (——).

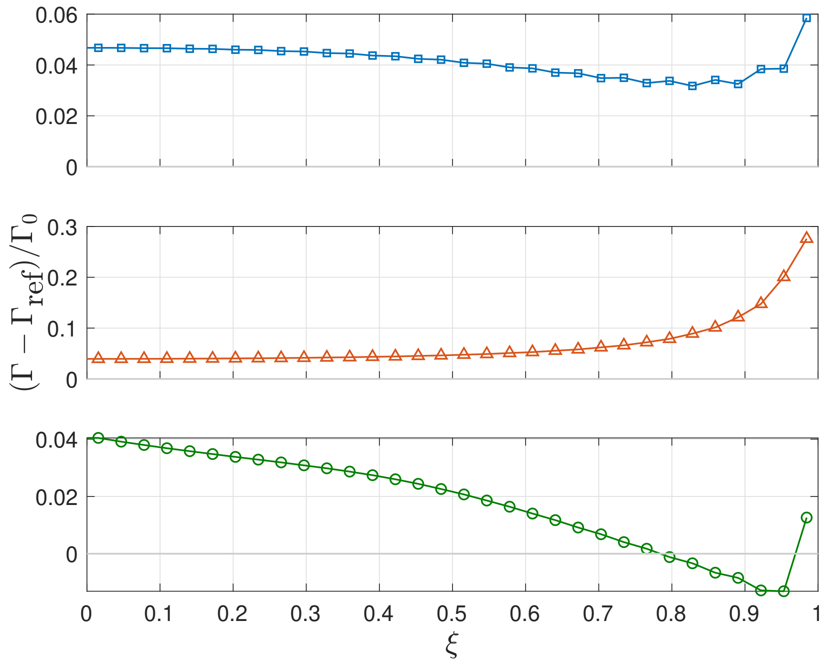

(a) Difference on the circulation distribution

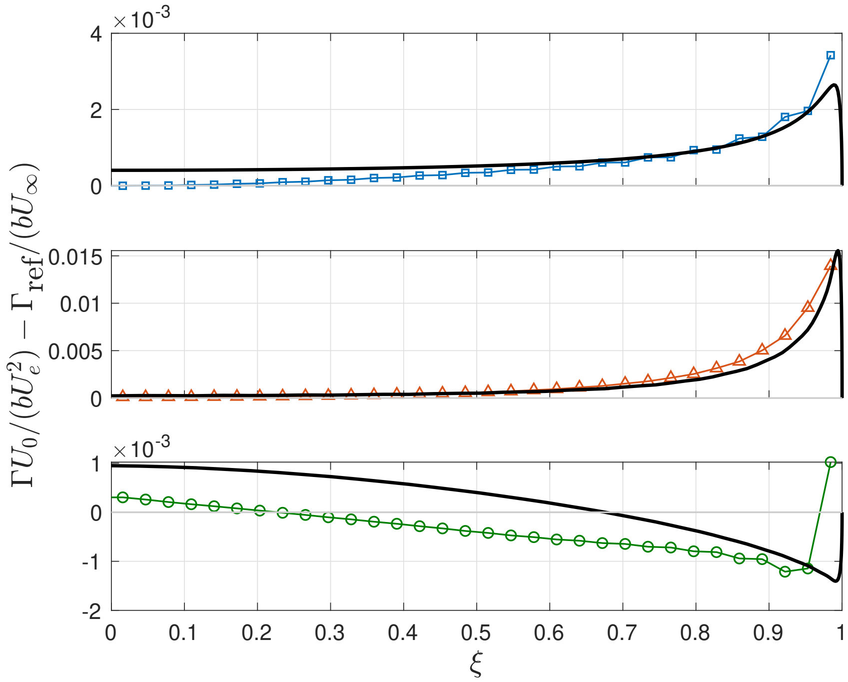

(b) Rescaled circulation distribution. The results from the 1-D mollified PLL with effective smoothing of $1.2\sigma_l/b$ are also presented (▬).

Fig. 13: Circulation distributions of Wings E (—□—), F (—△—) and G (—○—). For each wing, $\mathit{\Gamma}_{\text{ref}}$ is the respective circulation distribution obtained using the classical (singular) PLL.

profile drag is also four times smaller. This is to show that the method does not induce any static error. The low sensitivity of the results to the CFL number is also exemplified with results presented in Table 9. Notice that, if the wing was moving relatively to the mesh, one should use the relative velocity of the wing to evaluate the CFL condition.

	Wing	CFL	C_L			C_D		
			ILDL	CV	Δ	ILDL	CV	Δ
(t)	H	1	0.2533	0.2526	+0.0007	0.0269	0.0264	+0.0005
(u)	H	4	0.2519	0.2510	+0.0009	0.0270	0.0268	+0.0002

Table 9: Steady state lift and drag coefficients developed by the ILDL on wings H, using $h/b = 1/64$, layout I and $d/h = 3$, as evaluated by the ILDL model and as measured by the CV analysis.

In summary, even when the parasitic drag is included, the results of the ILDL are very much in line with the mollified PLL results. Also, the consistency between the forces evaluated on the ILDL and measured in the CV allows us to conclude that the vorticity structures in the wake are also faithfully generated and captured.

5 Application to the wake of an elliptical wing

The ILDL method implemented in the VPM solver is used to simulate the wake of an elliptical wing. This investigation aims to emphasize the role of the drag-induced vortical wake structures in the process of wake roll-up, and in the formation of a turbulent two vortex system (2-VS) in the far wake. For this purpose, the parasitic drag of the airfoil is set to three distinct values, leading to three high resolution simulations, with $\frac{h}{b} = \frac{1}{128}$ and $\frac{\sigma_l}{h} = \frac{\sigma_d}{h} = 1$ (layout II). The length of the simulation domains is extended to $L_x = 32b$. In terms of computational usage, each simulation was run on 1536 CPUs for fifteen hours, which corresponds to a physical time of $2L_x/U_\infty$.

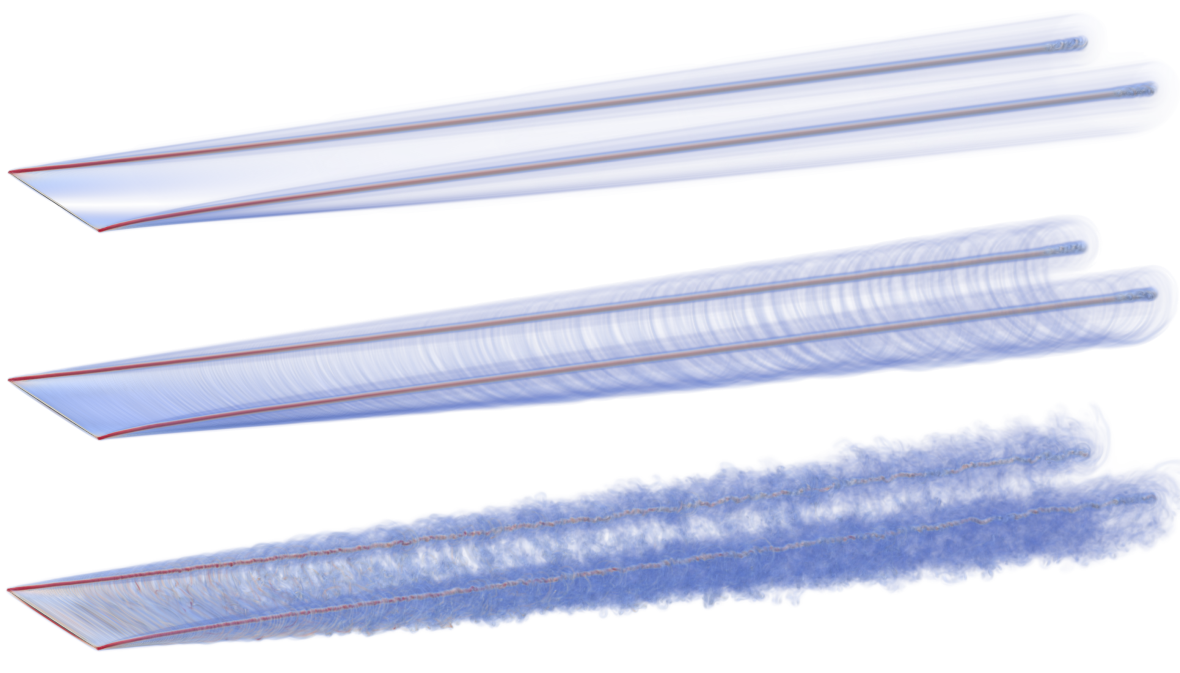

Fig. 14: Volume rendering of the magnitude of the vorticity shed in the wake of an elliptical wing at $C_L = 1$, respectively with no profile drag (top), a profile drag of $C_d = 0.03$ (center), and of $C_d = 0.1$ (bottom).

The wake vorticity is visualized in Fig. 14 for each drag setting. The first one has no parasitic drag. For the second one, the profile drag is set to $C_d = 0.03$ such that the wing parasitic drag (C_{D_0}) is close to the measured induced drag. This configuration thus corresponds to a wing flying at its maximum lift to drag ratio, as revealed by the polar of the wing $C_D = C_{D_0} + kC_L^2$, where the last term is the induced drag. In the last configuration, the profile drag is artificially increased to $C_d = 0.1$.

During the wake roll-up, the vortex sheet is stretched by the tip vortices and this eventually leads to the formation of a 2-VS. When there is no parasitic drag, that process is very smooth leading to straight, steady vortices. However, in the presence of profile drag, instabilities develop in the inboard region which is characterized by the velocity deficit associated to the parasitic drag. The stronger the drag, the larger the deficit and the quicker instabilities grow. Those also interact with the forming tip vortices. While the vortex cores remain very coherent in the case of none to moderate profile drag, they are subject to short-wavelength instabilities in the last configuration. The rolling-up vorticity then undergoes helical instabilities. Further downstream, the surrounding vorticity starts to generate small scale structures and the whole system eventually transitions to a turbulent state. By then, the SGS model (which is sensitive to the resolved small-scales vorticity field $\boldsymbol{\omega}_s$, Eq. (4)) has also become active.

The roll-up of the wakes is also shown in Fig. 15, using transverse slices at various locations downstream of the wing. The mean (i.e. time averaged) axial vorticity field exhibits the remnant of the vortex sheets at $\frac{x}{b} = 5$. At $\frac{x}{b} = 25$, the sheet is still visible for the case without drag, while it is more diffuse in the cases with parasitic drag. This confirms that the drag-induced vorticity contributes to the mixing in the wake.

In addition to vortex sheet instabilities during the roll-up, the drag is also responsible for a velocity deficit. In the near wake, it is observed all along the vortex structures, with a maximum at the center (the drag force was indeed maximum at the center of the wing). Further downstream, the velocity deficit tends to decrease, except in the vortex core where it increases, as the high velocity deficit regions have ben entrained there. It will of course eventually decrease, but this is not captured in the present simulation domain.

To conclude, these simulations show that the wake dynamics are mostly governed by the lift-induced components of the shed structures. However, the drag signature of the wing is responsible for additional instabilities and interactions which render the flow far more complex and in turn, accelerate the transition to turbulence in the wake, eventually leading to a fully developed turbulent 2-VS. The rate of the transition is of course related to the total parasitic drag of the wing.

6 Conclusions

In this article, the Immersed Lifting and Dragging Line (ILDL) method was introduced and shown to be an accurate and efficient method for the large eddy simulation of wake flows. The present approach is embedded in a hybrid Vortex Particle-Mesh (VPM) method. The ILDL computes the bound and shed vorticity corresponding to the local forces (lift and parasitic drag) developed by the modeled aerodynamic device. This vorticity is introduced in the flow using vortex particles, thus in a Lagrangian manner. Most importantly, the ILDL does not introduce an explicit mollification of the forces in the spanwise direction. Only a mollification of the vorticity in the transverse direction is required to guarantee the good numerical properties of the method. Furthermore, the Lagrangian framework allows for larger time steps than those imposed the classical CFL condition inherent to Eulerian methods (typically of the order of four times larger), thus helping to speed up the simulations. Both arguments were illustrated here.

Indeed, the verification of the ILDL method in the VPM solver showed a very good agreement with theory in the cases of airfoils and wings. In 3-D, the ILDL results were compared to those obtained using the classical (i.e. singular) Prandtl Lifting Line theory, and exhibited a first order convergence when the grid size was reduced. Additionally, the mollified Prandtl Lifting Line theory of [3] was used to verify that the influence of the vertical mollification was accurately captured in the present numerical implementation. In terms of circulation distribution, this mollification is responsible for a maximum relative difference of 5% near the tip, as compared to the classical PLL results, in the case of the elliptical wing; this difference rapidly decreases to roughly 1% further from the tip. Moreover, the obtained circulation distribution matches very accurately the results of the mollified PLL theory [3]. Other types of wings were also tested, and the influence of their shape on the distribution near the tip was quantified. Besides,

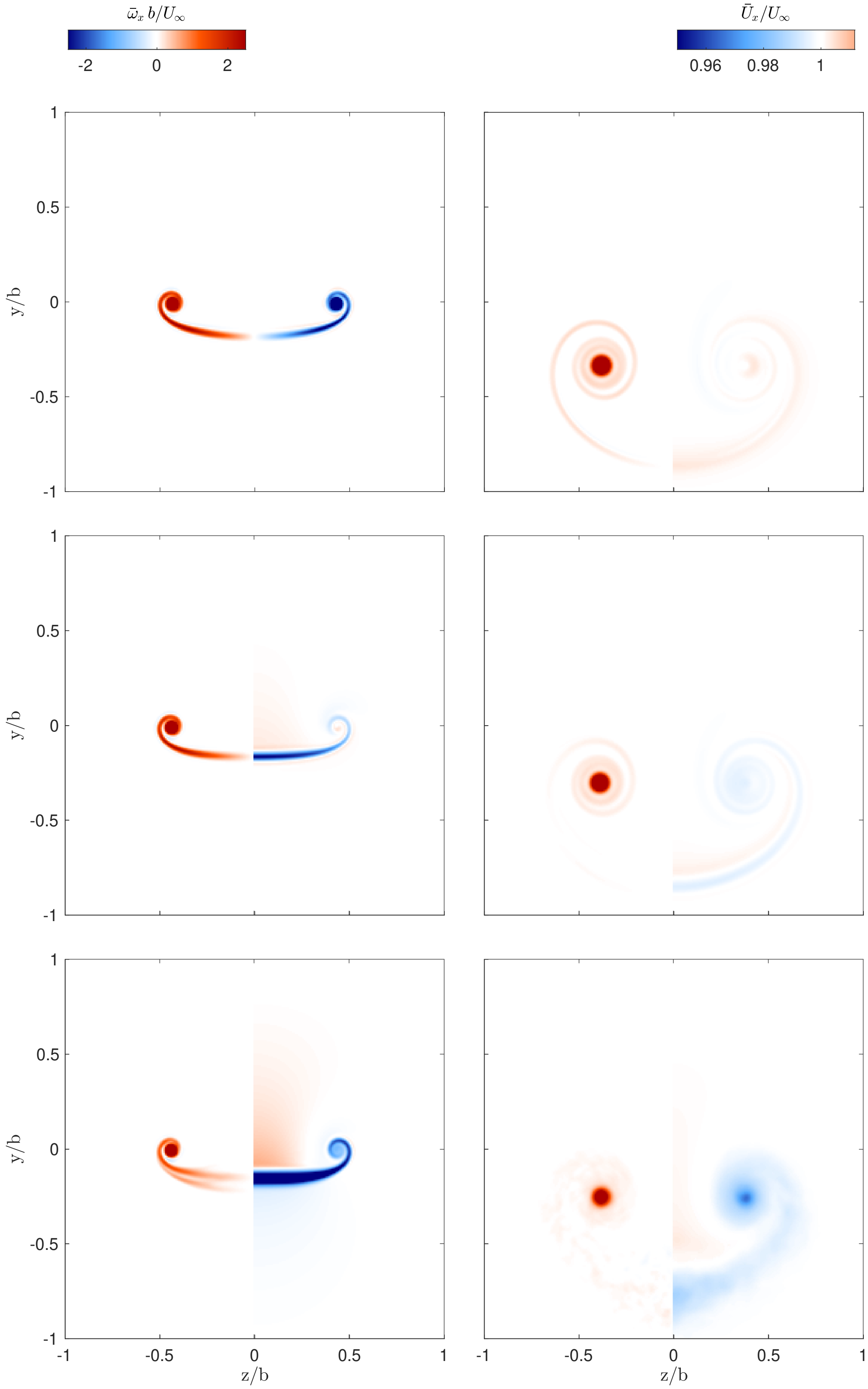

Fig. 15: Mean streamwise vorticity ($\bar{\omega}_x$) and velocity ($\bar{U}_x$) at $x/b = 5$ (left), and $x/b = 25$ (right), in the wake of an elliptical wing with no profile drag (top), $C_d = 0.03$ (center) and $C_d = 0.10$ (bottom).

the consistency between the forces computed by the ILDL method and the shed vorticity structures was systematically demonstrated using a control volume approach.

In addition to guaranteeing an efficient evaluation of the circulation distribution and the corresponding forces, the method is capable of tracking the associated vortical structures over very long distances. These qualities were illustrated through the simulation of the wake of an elliptical wing with three different parasitic drag settings, capturing the roll-up process and the formation of a two-vortex system in the far wake. Here, the drag induced vorticity structures were shown to be most important, accelerating the development of instabilities, and thus the transition to a turbulent flow.

To conclude, as wake flows are entirely governed by vortex dynamics and instabilities, the combination of the VPM solver and ILDL method proves to constitute a powerful approach for their study, as it is consistent with Prandtl theory, computationally efficient, and scalable to massively parallel frameworks. Even though the Actuator Line Model will likely remain the preferred method for LES of wind turbine wakes (one of the most researched topic in wake flows) in the near future, the authors believe that the present methodology can be considered as an interesting and efficient alternative and that it will bring insightful results for comparison with that mainstream approach. In that respect, the VPM solver with immersed lifting lines (no parasitic drag) has already demonstrated its great potential in several engineering applications, both in the context of fundamental academic research and within industrial research projects.

Appendix A. Reconstruction of the effective upstream velocity

In the presence of parasitic drag, the effective upstream velocity $\mathbf{U}_e$ differs from the measured $\mathbf{U}_0$. We here obtain the velocity induced by the dragging vortex sheets, which will be used as a correction velocity U_{corr} to recover the effective upstream velocity in the ILDL model: $U_e = U_0 - U_{\text{corr}}$.

First, we consider a 2-D steady, inviscid wake model with singular shed vortex sheets (Fig. 16) and an upstream velocity U_e. With small drag forces such as those experienced on airfoils, we reasonably assume that these vortex sheets remain parallel. Using the Biot-Savart law, the velocity evaluated at the center O of the dipole is

$$U_0 = U_e - \frac{\gamma}{2} = U_e - \frac{\mu}{2d}. \tag{17}$$

Using this expression to substitute μ in Eq. (10), we obtain

$$\left(\frac{U_0}{U_e}\right)^2 - \frac{U_0}{U_e} + \frac{C_d}{4}\frac{c}{d} = 0, \tag{18}$$

which provides the velocity correction factor

$$\frac{U_e}{U_0} = \frac{2}{1 + \sqrt{1 - C_d \frac{c}{d}}}. \tag{19}$$

The factor $C_d \frac{c}{d}$ plays an important role in this expression, and it is clear that it should be maintained well below unity for the correction to be valid.

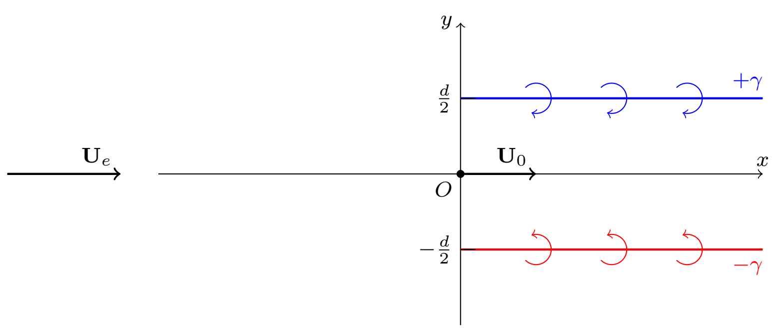

Fig. 16: Dragging dipole model centered at O and of width d

In the ILDL, the vortex sheets are regularized using a 1-D Gaussian regularization (of parameter σ_d) along y. The drag induced mollified vorticity field is

$$\begin{aligned}\omega_\sigma^d(x,y) &= \frac{\partial V_\sigma}{\partial x} - \frac{\partial U_\sigma}{\partial y}\\ &= \frac{\gamma}{\sqrt{\pi}\,\sigma_d} H(x) \left(\exp\left(-\frac{\left(y+\frac{d}{2}\right)^2}{{\sigma_d}^2} \right) - \exp\left(-\frac{\left(y-\frac{d}{2}\right)^2}{{\sigma_d}^2} \right) \right),\end{aligned} \tag{20}$$

where $H(x)$ is the Heavyside step function. As $\frac{\partial V_\sigma}{\partial x}$ is small, we obtain the horizontal velocity at $x=0$ as

$$U_\sigma^d(0,y) = -\int_{-\infty}^{y} \omega_\sigma(0,\zeta) d\zeta = -\frac{\gamma}{4} \left[\operatorname{erf}\left(\frac{y+\frac{d}{2}}{\sigma_d} \right) - \operatorname{erf}\left(\frac{y-\frac{d}{2}}{\sigma_d} \right) \right], \tag{21}$$

In case of pointwise velocity sampling, the correction U_{corr} is based on the evaluation of U_σ^d at $y=0$, and

$$U_e = U_0 - U_\sigma^d(0,0) = U_0 + \frac{\mu}{2d} \operatorname{erf}\left(\frac{d}{2\sigma_d} \right), \tag{22}$$

and we obtain, again using Eq. (10),

$$\frac{U_e}{U_0} = \frac{2}{1+\sqrt{1 - C_d \frac{c}{d} \operatorname{erf}\left(\frac{d}{2\sigma_d} \right)}}. \tag{23}$$

This is consistent with Eq. (19) when $\sigma_d \to 0$. We also make sure, in our simulations, that $C_d \frac{c}{d}$ is well below unity.

In the present work, we use the "integral velocity sampling" [3], i.e. the principal value obtained as $U_0 = \int \xi_{\sigma_l}(\mathbf{x}) U(\mathbf{x}) d\mathbf{x}$, where ξ_{σ_l} is the kernel used for the mollification of the bound vorticity, $\xi_{\sigma_l}(y) = \frac{1}{\sqrt{\pi}} \frac{1}{\sigma_l} \exp\left(-\frac{y^2}{\sigma_l^2} \right)$. Therefore, U_σ^d is used to derive an integrated correction,

$$U_e = \frac{1}{\sqrt{\pi}} \int_{-\infty}^{\infty} \exp\left(-\frac{y^2}{\sigma_l^2} \right) \left(U(0,y) - U_\sigma^d(0,y) \right) \frac{dy}{\sigma_l}. \tag{24}$$

In practice, this integral is evaluated numerically using the weights w_j of Table 1, where U is the velocity measured at the location of the bound vortex particles.

In general, $\mathbf{U}_0$ is not aligned with $\mathbf{U}_e$; the correction velocity should be aligned with the local shedding direction as shown in Fig. 2, and we use (24) in its vector form.

Appendix B. Errors related to the ILDL model assumptions

B.1 Error in drag evaluation, due to wake expansion

The expansion of the wake is neglected in the derivation of Eq. (8). This assumption generates a small error which can be quantified using Eq. (13).

Again, we use our simplified drag model made of two parallel singular vortex sheets (Fig. 16). As the vortex sheets are horizontal, the vertical velocity V across them is non zero. Consequently, there is a contribution to drag from the integral of $\mathbf{U} \wedge \boldsymbol{\omega}$. This contribution can be assimilated to the error introduced by neglecting the expansion of the wake.

The vertical velocity induced by the two vortex sheets is

$$\begin{aligned}V^d(x,y) &= \frac{\gamma}{2\pi} \int_0^\infty \left[\frac{(x-x')}{\left((x-x')^2 + (y-\frac{d}{2})^2\right)} - \frac{(x-x')}{\left((x-x')^2 + (y+\frac{d}{2})^2\right)} \right] dx'\\ &= -\frac{\gamma}{4\pi} \log\left(\frac{x^2 + (y-\frac{d}{2})^2}{x^2 + (y+\frac{d}{2})^2} \right).\end{aligned} \tag{25}$$

The model error in drag thus amounts to

$$\int \mathbf{U} \wedge \boldsymbol{\omega}\, d\mathbf{x} \cdot \hat{\mathbf{e}}_x = -\int_0^\infty V^d \gamma\, dx = \frac{\gamma^2}{2\pi} \int_0^\infty \log\left(\frac{x^2}{x^2+d^2} \right) dx = -\frac{\mu\gamma}{2}. \tag{26}$$

This term is proportional to the square of μ, and it is therefore indeed negligible for small drags.

B.2 Drag-induced lift

In the ILDL model, it is implicitly assumed that the effects of lift and drag can be added by linear superposition. In fact, even with wake expansion neglected, an interaction exists, which can be quantified again using the simple model of Fig. 16, to which we add a singular bound vortex of circulation Γ at O (similarly to what is presented in Fig. 2a).

As can be seen from Eq. (13), the integral of $\mathbf{U} \wedge \boldsymbol{\omega}$ will have a non-zero contribution from the combination of the axial velocity induced by the bound vortex and the circulation of the vortex sheets. The horizontal velocity induced by the bound vortex is

$$U^l(x,y) = \frac{\Gamma}{2\pi} \frac{y}{(x^2+y^2)} . \tag{27}$$

The interaction results in the appearance of some lift induced by drag,

$$\int \mathbf{U} \wedge \boldsymbol{\omega}\, d\mathbf{x} \cdot \hat{\mathbf{e}}_y = -2 \int_0^\infty U^l(x, \frac{d}{2})\, \gamma\, dx = -\frac{\Gamma\gamma}{\pi} \int_0^\infty \frac{\frac{d}{2}}{\left(x^2 + (\frac{d}{2})^2\right)} dx = -\frac{\Gamma\gamma}{2} . \tag{28}$$

When the mollification of the bound vortex and of the shed vortex sheets is taken into account, one can show that only a fraction of this term contributes to the drag-induced lift. The fraction depends on the values of $\frac{\sigma_l}{d}$ and $\frac{\sigma_d}{d}$, and it can be obtained numerically using the weights w_i.

The drag-induced lift, as computed here, could thus be accounted for in the ILDL model by modifying Eq. (7). However, in this work, it was decided to keep the model in its simplest form. The error associated to this simplification is quantified in the analysis of the validation results.

Appendix C. Fourier-based Poisson solver for domains with unbounded and inflow/outflow directions

In this work, we rely on the Fourier-based solvers used by [5,8] in order to solve Eq. (2) for the velocity. This solver handles a combination of periodic and unbounded directions through a Hockney-Eastwood approach [17] . We here extend that work to handle the unbounded directions together with the inflow and outflow conditions in the flow stream direction. Following [8], we re-write Eq. (2) as

$$\nabla^2_{yz} \mathbf{u} + \frac{\partial^2 \mathbf{u}}{\partial x^2} = -\nabla \wedge \boldsymbol{\omega} \ , \tag{29}$$

where x is assumed to be the inflow/outflow direction and ∇^2_{yz} is the Laplacian operator restricted to the $y-z$ plane. The Fourier-transform along x yields

$$\nabla^2_{yz} \tilde{\mathbf{u}} - k_x^2 \tilde{\mathbf{u}} = -\widetilde{\nabla \wedge \boldsymbol{\omega}} \ , \tag{30}$$

where $\tilde{\mathbf{u}}(k_x, y, z)$ stands for the x-transformed field. For a given k_x mode, this is a two-dimensional Helmholtz equation in an unbounded (y,z)-domain, which we can solve through the convolution with the Green's function

$$G^{2\mathrm{D}}_{\mathrm{i}|k_x|}(y,z) = \begin{cases} \frac{1}{2\pi} \ln(\sqrt{y^2+z^2}) & \text{if } k_x = 0 \,, \\ \frac{1}{2\pi} K_0 \left(|k_x| \sqrt{y^2+z^2} \right) & \text{otherwise} \,, \end{cases} \tag{31}$$

where K_0 denotes the modified Bessel function of the second kind. These expressions are singular at $(y,z) = (0,0)$. This is here circumvented by replacing them with the corresponding cell-averaged value [8], but we could alternatively use a mollified Helmholtz kernel [15,16,42]. The convolution itself can be carried out in Fourier space through the domain-doubling approach of [17].

In such a context, the imposition of inflow/outflow conditions simply corresponds to a restriction of the Fourier modes to be considered, depending on the symmetry conditions that needs to be enforced on each side of the domain. We assume the domain to go from 0 to L_x in x. Considering the velocity field, we wish to impose the following conditions on the streamwise velocity: $u_x(0,y,z) = u_x(L_x,y,z) = U_\infty$. This corresponds to odd symmetry conditions on $\mathbf{u}_{\boldsymbol{\omega}}$ at the inflow and at the outflow. These are completed with even symmetry conditions on the transverse components $\frac{\partial u_y}{\partial x}(0,y,z) = \frac{\partial u_z}{\partial x}(0,y,z) = 0$ and $\frac{\partial u_y}{\partial x}(L_x,y,z) = \frac{\partial u_z}{\partial x}(L_x,y,z) = 0$. The allowed modes thus have to be harmonics of a base mode of period $2L_x$ with the proper phase

$$u_x = U_\infty + \sum_i \sin\left(i\pi \frac{x}{L_x}\right) \tilde{u}_x \left(\frac{i\pi}{L_x}, y, z\right) \ , \tag{32}$$

$$u_{(y,z)} = \sum_i \cos\left(i\pi \frac{x}{L_x}\right) \tilde{u}_{(y,z)} \left(\frac{i\pi}{L_x}, y, z\right) \ . \tag{33}$$

The modes of the corresponding vorticity field are then

$$\omega_x = \sum_i \cos\left(i\pi \frac{x}{L_x}\right) \tilde{\omega}_x \left(\frac{i\pi}{L_x}, y, z\right) \ , \tag{34}$$

$$\omega_{(y,z)} = \sum_i \sin\left(i\pi \frac{x}{L_x}\right) \tilde{\omega}_{(y,z)} \left(\frac{i\pi}{L_x}, y, z\right) \ . \tag{35}$$

Notice that, in general, any combination of symmetry conditions is accessible and it leads to domains with a periodicity of either 2 or 4 times L_x.

The practical implementation of this restriction is made straightforward through the use of Discrete Sine and Cosine transforms (DCT and DST) in our FFT-based solver. Advantageously, and unlike the domain-doubling technique for the unbounded directions, this implementation does not lead to a twofold (or fourfold) increase in the unknowns as the DCT/DST transforms are performed in the domain with its original L_x size.

Acknowledgements The development work benefited from the computational resources provided by the supercomputing facilities of the Université catholique de Louvain (CISM/UCL) and the Consortium des Équipements de Calcul Intensif en Fédération Wallonie Bruxelles (CÉCI) funded by the Fond de la Recherche Scientifique de Belgique (F.R.S.-FNRS) under Convention No. 2.5020.11. The production simulations used computational resources made available on the Tier-1 supercomputer of the Fédération Wallonie-Bruxelles, infrastructure funded by the Walloon Region under the Grant Agreement No. 1117545.

References

1. Breton, S.P., Sumner, J., Sørensen, J.N., Hansen, K.S., Sarmast, S., Ivanell, S.: A survey of modelling methods for high-fidelity wind farm simulations using large eddy simulation. Phil. Trans. R. Soc. A **375**(2091), 20160097 (2017)
2. Caprace, D.G., Buffin, S., Duponcheel, M., Chatelain, P., Winckelmans, G.: Large Eddy Simulation of Advancing Rotor for Near to Far Wake Assessment. In: 43rd European Rotorcraft Forum, p. 570. Milan, Italy (2017)
3. Caprace, D.G., Chatelain, P., Winckelmans, G.: Lifting line with various mollifications: Theory and application to an elliptical wing. AIAA Journal **57**(1), 1–12 (2019)
4. Chatelain, P., Backaert, S., Winckelmans, G., Kern, S.: Large Eddy Simulation of wind turbine wakes. In: W. Rodi (ed.) Proceedings of The 9th International Symposium on Engineering Turbulence Modelling and Measurements (ETMM-9), June 6–8, 2012, Thessaloniki, Greece, *Flow, Turbulence and Combustion*, vol. 91, pp. 587–605. ERCOFTAC, Springer (2013). DOI 10.1007/s10494-013-9474-8
5. Chatelain, P., Curioni, A., Bergdorf, M., Rossinelli, D., Andreoni, W., Koumoutsakos, P.: Billion vortex particle Direct Numerical Simulations of aircraft wakes. Computer Methods in Applied Mechanics and Engineering **197**(13), 1296–1304 (2008). DOI 10.1016/j.cma.2007.11.016
6. Chatelain, P., Duponcheel, M., Caprace, D.G., Marichal, Y., Winckelmans, G.: Vortex particle-mesh simulations of vertical axis wind turbine flows: from the airfoil performance to the very far wake. Wind Energy Science **2**(1), 317 (2017). DOI 10.5194/wes-2-317-2017
7. Chatelain, P., Duponcheel, M., Zeoli, S., Buffin, S., Caprace, D.G., Winckelmans, G., Bricteux, L.: Investigation of the effect of inflow turbulence on vertical axis wind turbine wakes. Journal of Physics: Conference Series **854**(1), 012011 (2017). DOI 10.1088/1742-6596/854/1/012011
8. Chatelain, P., Koumoutsakos, P.: A Fourier-based elliptic solver for vortical flows with periodic and unbounded directions. Journal of Computational Physics **229**(7), 2425–2431 (2010)
9. Churchfield, M.J., Schreck, S., Martinez-Tossas, L.A., Meneveau, C., Spalart, P.R.: An Advanced Actuator Line Method for Wind Energy Applications and Beyond. In: 35th Wind Energy Symposium, p. 1998 (2017)
10. Cocle, R., Bricteux, L., Winckelmans, G.: Scale dependence and asymptotic very high Reynolds number spectral behavior of multiscale subgrid models. Physics of Fluids **21**(8), 085101 (2009). DOI 10.1063/1.3194302
11. Cocle, R., Winckelmans, G., Daeninck, G.: Combining the vortex-in-cell and parallel fast multipole methods for efficient domain decomposition simulations. Journal of Computational Physics **227**(21), 9091–9120 (2008). DOI 10.1016/j.jcp.2007.10.010
12. Cottet, G.H., Koumoutsakos, P.: Vortex Methods, Theory and Practice. Cambridge University Press (2000)
13. Dag, K.: Combined pseudo-spectral / actuator line model for wind turbine applications. Ph.D. thesis, Technical University of Denmark (2017)
14. Hallock, J.N., Holzäpfel, F.: A review of recent wake vortex research for increasing airport capacity. Progress in Aerospace Sciences **98**, 27–36 (2018). DOI 10.1016/j.paerosci.2018.03.003
15. Hejlesen, M., Rasmussen, J., Chatelain, P., Walther, J.: A high order solver for the unbounded Poisson equation. Journal of Computational Physics **252**, 458–467 (2013). DOI 10.1016/j.jcp.2013.05.050
16. Hejlesen, M.M., Winckelmans, G., Walther, J.H.: Non-singular green's functions for the unbounded poisson equation in one, two and three dimensions. Applied Mathematics Letters **89**, 28–34 (2019). DOI 10.1016/j.aml.2018.09.012.
17. Hockney, R., Eastwood, J.: Computer Simulation using Particles. Taylor & Francis, Inc. Bristol, PA, USA (1988)
18. Ivanell, S., Sorensen, J.N., Mikkelsen, R., Henningson, D.: Analysis of Numerically Generated Wake Structures. Wind Energy **12**(1), 63–80 (2009). DOI 10.1002/we.285
19. Jeanmart, H., Winckelmans, G.: Investigation of eddy-viscosity models modified using discrete filters: A simplified regularized variational multiscale model and an enhanced field model. Physics of Fluids **19**(5), 055110 (2007). DOI 10.1063/1.2728935
20. Jha, P.K., Churchfield, M.J., Moriarty, P.J., Schmitz, S.: Guidelines for Volume Force Distributions Within Actuator Line Modeling of Wind Turbines on Large-Eddy Simulation-Type Grids. Journal of Solar Energy Engineering **136**(3), 031003–031003 (2014)
21. Jha, P.K., Schmitz, S.: Actuator curve embedding – an advanced actuator line model. Journal of Fluid Mechanics **834** (2018). DOI 10.1017/jfm.2017.793
22. Katz, J., Plotkin, A.: Low-speed aerodynamics, vol. 13. Cambridge university press (2001)
23. Koumoutsakos, P.: Inviscid axisymmetrization of an elliptical vortex. Journal of Computational Physics **138**(2), 821–857 (1997). DOI 10.1006/jcph.1997.5749

24. Lee, S.J.: Numerical Simulation of Vortex-Dominated Flows Using the Penalized VIC Method, pp. 151–182. InTech (2017)
25. Martínez-Tossas, L., Churchfield, M., Meneveau, C.: Optimal smoothing length scale for actuator line models of wind turbine blades based on Gaussian body force distribution. Wind Energy (2017)
26. Martínez-Tossas, L.A., Meneveau, C.: Filtered lifting line theory and application to the actuator line model. Journal of Fluid Mechanics **863**, 269–292 (2019). DOI 10.1017/jfm.2018.994
27. Meyer Forsting, A.R., Pirrung, G.R., Ramos-García, N.: A vortex-based tip/smearing correction for the actuator line. Wind Energy Science (2019). DOI 10.5194/wes-2018-76
28. Mimeau, C., Cottet, G.H., Mortazavi, I.: Direct numerical simulations of three-dimensional flows past obstacles with a vortex penalization method. Computers & Fluids **136**, 331 – 347 (2016). DOI 10.1016/j.compfluid.2016.06.020.
29. Moens, M., Duponcheel, M., Winckelmans, G., Chatelain, P.: An actuator disk method with tip-loss correction based on local effective upstream velocities. Wind Energy **21**(9), 766–782 (2018)
30. Monaghan, J.: Extrapolating B splines for interpolation. Journal of Computational Physics **60**(2), 253 – 262 (1985). DOI 10.1016/0021-9991(85)90006-3
31. Noca, F., Shiels, D., Jeon, D.: A comparison of methods for evaluating time-dependent fluid dynamic forces on bodies, using only velocity fields and their derivatives. Journal of Fluids and Structures **13**(5), 551–578 (1999)
32. Phillips, W., Snyder, D.: Modern adaptation of Prandtl's classic lifting-line theory. Journal of Aircraft **37**(4), 662–670 (2000)
33. Ploumhans, P., Winckelmans, G.S.: Vortex Methods for High-Resolution Simulations of Viscous Flow Past Bluff Bodies of General Geometry. Journal of Computational Physics **165**(2), 354–406 (2000)
34. Prandtl, L.: Tragflügeltheorie, pp. 451–477. Göttinger Nachrichten, Mathematisch- Physikalische Klasse, Germany (1918)
35. Rasmussen, J.T., Cottet, G.H., Walther, J.H.: A multiresolution remeshed Vortex-In-Cell algorithm using patches. Journal of Computational Physics **230**, 6742–6755 (2011)
36. van Rees, W.M., Leonard, A., Pullin, D.I., Koumoutsakos, P.: A comparison of vortex and pseudo-spectral methods for the simulation of periodic vortical flows at high Reynolds numbers. Journal of Computational Physics **230**(8), 2794–2805 (2011)
37. Sbalzarini, I.F., Walther, J.H., Polasek, B., Chatelain, P., Bergdorf, M., Hieber, S.E., Kotsalis, E.M., Koumoutsakos, P.: A software framework for the portable parallelization of particle-mesh simulations (2006)
38. Scheurich, F.: Modelling the aerodynamics of vertical-axis wind turbines. Ph.D. thesis, University of Glasgow (2011)
39. Shives, M., Crawford, C.: Mesh and load distribution requirements for actuator line cfd simulations. Wind Energy **16**(8), 1183–1196 (2013)
40. Sorensen, J.N., Shen, W.Z.: Numerical modeling of wind turbine wakes. Journal of Fluids Engineering - Transactions of the ASME **124**(2), 393–399 (2002). DOI 10.1115/1.1471361
41. Spalart, P.R.: On the far wake and induced drag of aircraft. Journal of Fluid Mechanics **603**, 413–430 (2008). DOI 10.1017/S0022112008001146
42. Spietz, H.J., Hejlesen, M.M., Walther, J.H.: A regularization method for solving the poisson equation for mixed unbounded-periodic domains. Journal of Computational Physics **356**, 439 – 447 (2018). DOI 10.1016/j.jcp.2017.12.018.
43. Tollmien, W., Schlichting, H., Görtler, H.: Über Tragflügel kleinsten induzierten Widerstandes. In: Ludwig Prandtl Gesammelte Abhandlungen, pp. 556–561. Springer (1961)
44. Voutsinas, S.G.: Vortex methods in aeronautics: how to make things work. International Journal of Computational Fluid Dynamics **20**(1), 3–18 (2006). DOI 10.1080/10618560600566059
45. Winckelmans, G.S.: Encyclopedia of Computational Mechanics, chap. Vortex Methods, pp. 129–153. John Wiley & Sons, Ltd (2004). DOI 10.1002/0470091355.ecm055